Effective conditions for the reflection of an acoustic wave by low-porosity perforated plates

Sophie Laurens, Estelle Piot, Abderrahmane Bendali, M'Barek Fares, Sébastien Tordeux

Effective conditions for the reflection of an acoustic wave by low-porosity perforated plates

S. LAURENS[1,3]†, E. PIOT[2], A. BENDALI[1,3], M'B. FARES[3], AND S. TORDEUX[4]

[1]IMT, University of Toulouse, INSA, 135 avenue de Rangueil, F-31077, Toulouse, France

[2]ONERA - The French Aerospace Lab, F-31055, Toulouse, France

[3]CERFACS, 42 avenue Gaspard Coriolis, F-31100, Toulouse, France

[4] INRIA & University of Pau, LMA, avenue de l'Université, F-64000, Pau, France

(Received ?; revised ?; accepted ?. - To be entered by editorial office)

This paper describes an investigation of the acoustic properties of a low-porosity perforated plate in a compressible ideal inviscid fluid in the absence of mean flow. The study shows in particular how the reflection and transmission coefficients of an acoustic plane wave produced by such a device can be expressed in terms of the Rayleigh conductivity of an isolated perforation by extending the approach introduced for the case of thick plates by Leppington and Levine, *Reflexion and transmission at a plane screen with periodically arranged circular or elliptical apertures*, J. Fluid Mech., 1973, p.109-127. Lower and upper bounds for the Rayleigh conductivity of a perforation in a thick plate are usually derived from intuitive approximations and by reasoning based on physical observation. The paper addresses a mathematical justification of these approaches, yielding accurate bounds for various geometries, untilted or tilted, with a conical shape or an elliptical section. Accurate estimates of the Rayleigh conductivity for a single perforation have a direct impact on the precision of models used for predicting the acoustic behavior of a perforated plate mainly on the basis of its reflection and transmission coefficients. It is shown in this paper how asymptotic expansions can be used to derive first and second-order accurate, albeit approximate expressions of these coefficients, as well as of the effective compliance of the perforated plate.

Key words:

1. Introduction

Perforated plates and screens are widely used in engineering systems due to their ability to absorb sound or to reduce sound transmission, in a variety of applications including room acoustics and aeroacoustics (Ingard 1994; Beranek 1992). They can be used as protective layers of porous materials (Allard 1993), to form sandwich structures in aircraft fuselages (Abrahams 1999) or as facing layers of liners. In this case, the perforated plates are either backed by honeycomb cells which are mounted on a rigid backplate (Maa 1998) or by a plenum acting as a resonant cavity in gas turbine combustion chambers (Lefebvre 1999).

The reflection and transmission properties of such perforated panels can be modeled

† Email address for correspondence: sophie.laurens@cerfacs.fr

directly, as was done by Leppington & Levine (1973) by means of an integral equation or later by the method of matched asymptotic expansions (see Bendali *et al.* (2012) and Leppington (1990) for the case of elastic plates). The Leppington and Levine approach was later extended by Howe (1980) and Dowling & Hughes (1992) to include a mean tangential or bias flow to the perforated screen. In these papers, the asymptotic solution is sought in the long wavelength limit, i.e., the size of each perforation is assumed to be small in comparison with the distance between two neighbouring apertures, viewed in turn as being much smaller than the wavelength of the impinging sound waves.

While the acoustic behaviour of an aperture can be modeled in various way, depending on the actual problem being considered, the acoustic effect of perforated plates is usually addressed by studying the acoustic behaviour of a single aperture in an infinite wall and by designing a homogeneous model for the whole plate, mainly by means of an averaging procedure. In the studies for aeronautical turbofan engines (see for example Tam *et al.* 2008, for a recent review), the acoustic impedance is the relevant parameter, more precisely, the ratio of the fluctuating pressure across the hole to the normal fluctuating velocity through it. The real part of the impedance is denoted as a resistance and its imaginary part as a reactance. On the contrary, with respect to gas turbines (see Andreini *et al.* 2011; Scarpato *et al.* 2012, for instance), the acoustic behaviour of the aperture is described in terms of its compliance, termed in this context 'Rayleigh conductivity', which characterizes the fluctuating volume flow rate through the hole as a function of the difference in unsteady pressure between each side of the plate.

The physical phenomenon involved in the acoustic behaviour of an aperture can be broken down into three mechanisms. The first one is purely inviscid and is associated with the sound radiation of the perforation and the distortion of the acoustic flow at the plate surface. This flow can be assumed to be potential and governed by the linearized Helmholtz equation, under the assumption that a characteristic size of the hole is small in comparison with the acoustic wavelength. Consequently, no acoustic damping can be predicted by this approach, which means that the impedance Z of the aperture is purely imaginary, while its Rayleigh conductivity K_R is purely real. This mechanism is generally explained by considering that the flow within the hole behaves as a small piston of air, whose thickness is larger than the neck depth because of inertial effect. This amounts to increasing the mass of the vibrating air and is accounted for using correction lengths, which need to be added to the plate thickness. For a circular aperture of radius r, Rayleigh (1945) gave a lower and an upper bound for this end correction: $\pi r/2 \approx 1.57r$ and $16r/3\pi \approx 1.70r$. Later, Morfey (1969) derived approximated expressions for openings of arbitrary shape at low frequencies. The second mechanism is linked to viscous effects occurring within the viscous boundary layers which develop at the perforation's inner walls, and around the perforation edges at the plate surface. This induces a real part for the acoustic impedance (i.e., an imaginary part of the Rayleigh conductivity), which is linked to an absorption of acoustic energy. Viscous effects also modify the imaginary part of the impedance, which is usually modeled by viscous end corrections (Melling 1973; Maa 1998).

Finally, the third mechanism consists of vortex shedding, which converts acoustical into mechanical energy, subsequently dissipated into heat. This may be due to nonlinear effects, when high-amplitude sound waves impinge on the aperture in the absence of mean flow (Cummings 1984), or to the effect of mean flow. In the presence of a grazing mean flow, empirical (Guess 1975; Kirby & Cummings 1998), semi-empirical (Cummings 1986, 1987) or analytical (Howe 1996) models are used to find the impedance or the Rayleigh conductivity of the aperture. It is shown that the resistance induced by a high-speed grazing flow is much larger than the viscous resistance obtained without

flow, consequently an increased loss of acoustic power is generally observed. However the phenomena involved are quite complex and has not been accurately and comprehensively modelled. On the contrary, when the perforation is subject to a bias flow, even when mechanisms similar to the grazing case are involved, Howe (1979) developed an analytical model for the aperture Rayleigh conductivity which proved to be quite reliable (Hughes & Dowling 1990; Jing & Sun 1999; Eldredge & Dowling 2003; Bellucci *et al.* 2004; Mendez & Eldredge 2009; Scarpato *et al.* 2012). It consists in multiplying the no-flow Rayleigh conductivity of a zero-thickness circular aperture (taken equals to $K_R = 2r$, i.e., an inertial end correction of $\pi r/2$) by a complex function of the mean bias flow Mach number. The Reynolds number within the perforation is assumed to be large enough so that viscous effects can be neglected except near the edges, where flow separation takes place. Later, this model was improved to take into account the perforation thickness, by adding it to the inertial end correction (Jing & Sun 2000) or by modifying the flow-dependent function (Luong *et al.* 2005). However these expressions only deal with the simplified geometry of a non-tilted circular aperture, while in actual combustors the apertures are tilted downstream and their cross-section in the plate plane is elliptical. Recent papers have numerically (Eldredge *et al.* 2007) or experimentally (Andreini *et al.* 2011) investigated such a realistic geometry, by using Howe's model with a modified thickness and by neglecting some other geometric effects. Finally, only a few studies have addressed the acoustic response of a perforation in the complex configuration where an exiting bias flow interacts with a grazing flow, except for the work of Sun *et al.* (2002), who attempted to correlate experimental results with an empirical model.

If the distance between two successive holes of a perforated plate is sufficiently great when compared to the size of each perforation and if the ratio of this distance to the wavelength is sufficiently small, the device behaves acoustically as though each perforation were isolated. In this case, the Rayleigh conductivity (or impedance) of a single aperture, as defined above, is used to define an expression for the compliance (or impedance) of a homogeneous screen of such apertures, by assuming that the fluctuating volume flux through each hole is uniformly distributed over each cell of the array of perforations (see Eldredge & Dowling 2003; Hughes & Dowling 1990; Melling 1973; Maa 1998; Atalla & Sgard 2007). The layout of the array of holes is not involved in any way. When the porosity σ of the perforated plate is greater than about 4%, interaction between the apertures can no longer be neglected. The problem of acoustic interaction was solved by Fok (1941) for the case of an infinitely thin plate with circular perforations. He derived a modified Rayleigh conductivity defined as $K'_R = 2r\psi(\sqrt{\sigma})$. Melling (1973) used Fok's function ψ for modifying the inertial end correction (taken equal to $16r/3\pi$ in his model) while other authors (Guess 1975; Beranek 1992; Allard 1993) preferred to use empirical expressions. Recently, interaction effects were studied numerically and experimentally by Lee *et al.* (2007) for the case of perforated plates with a bias flow.

In this paper, we focus on a few questions arising from the previous discussion. First, it was shown that all the impedance or conductivity models are based on the inertial end corrections given by Rayleigh (1945) for a single circular aperture in an infinitely thin plate. It should be noted that in room acoustics and liner applications, it is the $16r/3\pi$ bound which is used, seemingly introduced by Ingard (1953). On the contrary, Howe's model (Howe 1979) with an end correction of $\pi r/2$ seems to be the one most widely used in papers dealing with gas turbines. The aim of the present paper is to provide a rigorous mathematical framework in order to derive accurate bounds of the inertial end correction. This will makes it possible to determine these bounds for complex geometries of the perforation, especially when the aperture is thick, tilted and has a circular bore, as in gas turbine problems. Finally, we shall see how the Leppington and Levine method

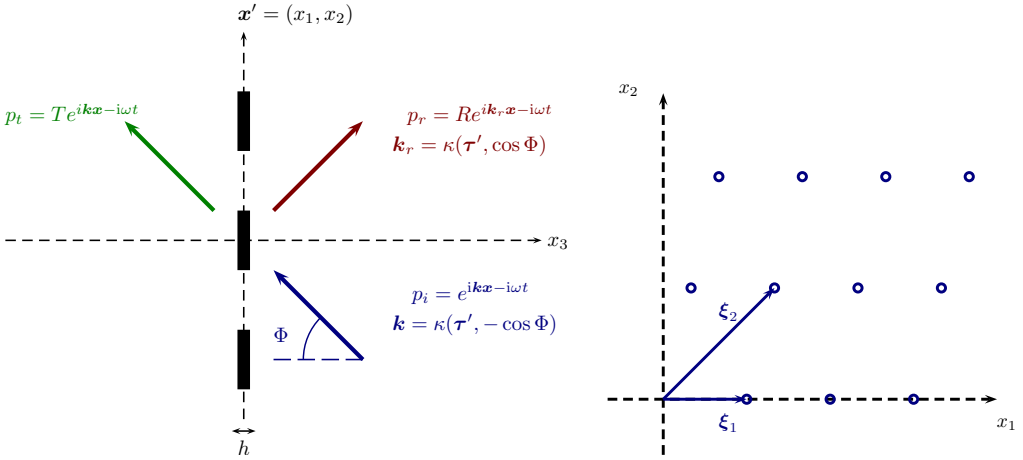

(a) Incident and scattered acoustic waves

(b) Sketch showing layout of the holes in the lattice

Figure 1: The geometry of the perforated screen

can be adapted to deal with such configurations while at the same time obtaining some second-order terms for approximation of the effective compliance of the plate.

2. Description of the perforated plate and governing equations

Consider the situation shown in figure 1 of a perforated screen in a compressible ideal inviscid fluid in the absence of mean flow. A time-periodic acoustic plane wave is obliquely incident to an infinitely rigid plate of thickness h that lies in the plane $x_3 = 0$ (see figure 1a) at an angle Φ to the normal direction to the plate, with $-\pi/2 < \Phi < \pi/2$. Throughout the paper, the coordinate system $\boldsymbol{x}$ is decomposed into the two-dimensional variable $\boldsymbol{x}' = (x_1, x_2)$ and the coordinate along the normal to the plate x_3. The pressure variation of the incident wave is given by

$$p_i = \exp\left(\mathrm{i}\kappa(\boldsymbol{\tau}' \cdot \boldsymbol{x}' - x_3 \cos\Phi) - \mathrm{i}\omega t\right) \tag{2.1}$$

with $\boldsymbol{\tau} = (\boldsymbol{\tau}', -\cos\Phi)$ the cosine directors of the direction of propagation. The wavenumber $\kappa = \omega/c_0$ expresses the ratio of the angular frequency ω to the speed of sound c_0. At a great enough distance from the perforated plate, the scattered pressure field can be decomposed into a reflected wave

$$p_r = R\, \exp\left(\mathrm{i}\kappa(\boldsymbol{\tau}' \cdot \boldsymbol{x}' + x_3 \cos\Phi) - \mathrm{i}\omega t\right) \tag{2.2}$$

and a transmitted one

$$p_t = T\, \exp\left(\mathrm{i}\kappa(\boldsymbol{\tau}' \cdot \boldsymbol{x}' - x_3 \cos\Phi) - \mathrm{i}\omega t\right) \tag{2.3}$$

where R and T are complex constants, which depend on the acoustic properties of the perforated plate. The time multiplicative factor $e^{-\mathrm{i}\omega t}$ is hereafter suppressed by linearity.

In the fluid domain, the pressure field satisfies the homogeneous Helmholtz equation and the cancellation of normal velocity on the rigid walls, equivalently expressed from the linearized momentum equation, by cancelling the pressure normal derivative. Thus,

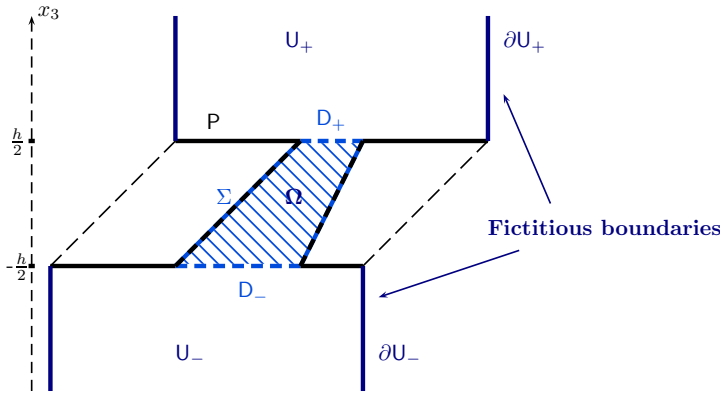

Figure 2: Schematic view of the lattice unit cell. The aperture is depicted by the blue dashed area, the walls of the plate are plotted in thick black lines.

the acoustic wave is governed by the following boundary-value problem:

$$\begin{cases} \nabla^2 p + \kappa^2 p = 0 & \text{in the fluid domain} \\ \partial_{\boldsymbol{n}} p = 0 & \text{on the rigid walls} \\ p = p_i + p_r & \text{as } x_3 \to +\infty \\ p = p_t & \text{as } x_3 \to -\infty \end{cases} \tag{2.4}$$

The perforated plate contains a two-dimensional doubly-periodic lattice of arbitrary-shaped apertures, with centres at the points

$$\boldsymbol{\xi}_m = m_1 \boldsymbol{\xi}_1 + m_2 \boldsymbol{\xi}_2, \tag{2.5}$$

where $m = (m_1, m_2)$ is a pairing of two integers and $\boldsymbol{\xi}_i$ are the periodicity vectors of the lattice (see figure 1b). The surface of the unit lattice cell is $A = |\boldsymbol{\xi}_1 \times \boldsymbol{\xi}_2|$ and the spacing between two successive perforations is denoted by $L = \max(|\boldsymbol{\xi}_1|, |\boldsymbol{\xi}_2|)$.

The acoustic wavelength $2\pi/\kappa$ is assumed to be large in comparison with the aperture size, however the spacing parameters $|\boldsymbol{\xi}_1|$ and $|\boldsymbol{\xi}_2|$ are only required to be less than half a wavelength (see (Bendali *et al.* 2012))

$$L < \lambda/2. \tag{2.6}$$

This ensures that only the fundamental mode, corresponding to $m_1 = m_2 = 0$, is propagating for any incident wave. All the short-range interaction effects between the apertures are neglected, i.e. acoustically, the plate is assumed to be of low-porosity.

As depicted in figure 2, each aperture of the perforated plate consists of a bounded domain Ω located between the two planes $x_3 = -h/2$ and $x_3 = h/2$. The lower and upper openings of the perforation are denoted by D_- and D_+ and its lateral part by Σ. It is convenient to consider the decomposition of domain U within the unit cell into non-overlapping domains, filled by the fluid consisting of, respectively, the lower and upper semi-infinite tubes U_- and U_+ and the hole Ω. The lateral parts of the boundaries of, respectively, U_-, U_+ and Ω will be denoted as $\partial\mathsf{U}_-$, $\partial\mathsf{U}_+$ and $\partial\Omega$. Conveniently, we consider the following local coordinate systems of respectively $\mathsf{U}^\pm$:

$$\boldsymbol{x}_\pm = (\boldsymbol{x}'_\pm, x_3^\pm) \quad \text{with } x_3^+ \geqslant 0 \text{ and } x_3^- \leqslant 0. \tag{2.7}$$

Because the acoustic wavelength is large as compared with the aperture size, each aperture can be considered as acoustically compact. This means that the local motion

through an aperture is assumed to be incompressible:

$$\boldsymbol{\nabla} \cdot \boldsymbol{v} = 0 \quad \text{in } \Omega, \tag{2.8}$$

where $\boldsymbol{v}$ is the acoustic velocity field. As a result, the governing equations (2.4) can be expressed in terms of a potential:

$$\begin{cases} \nabla^2 p = 0 & \text{in } \mathsf{U} \\ \partial_{\boldsymbol{n}} p = 0 & \text{on the rigid walls} \\ \lim_{|\boldsymbol{x}|\to\pm\infty} p = P^{\pm}, & \end{cases} \tag{2.9}$$

where P^+ and P^- are limiting values of pressure at big distance from the aperture. By identification with (2.1), (2.2) and (2.3), we have $P^+ = p_i + p_r$ and $P^- = p_t$. Under this assumption, the Rayleigh conductivity of the aperture is defined as (Howe 1998):

$$K_R = \frac{\mathrm{i}\omega\rho_0 Q}{P^+ - P^-}, \tag{2.10}$$

where ρ_0 denotes the mean density of the fluid and Q is the volume flux through the aperture in the x_3 direction : $Q = \int_{D_+} v_3 \,\mathrm{d}x_1\mathrm{d}x_2 = \int_{D_-} v_3 \,\mathrm{d}x_1\mathrm{d}x_2$. Using the linearized momentum equation, the Rayleigh conductivity can be expressed as a function of pressure only:

$$K_R = \frac{1}{P^+ - P^-} \int_{D_+} \partial_{x_3} p \,\mathrm{d}\boldsymbol{x}'. \tag{2.11}$$

3. Rayleigh conductivities for thick plates with holes having complex geometries

In this section, we propose a rigorous method for estimating the Rayleigh conductivity of thick plates. This method matches Howe's estimates for cylindrical and conical untilted perforations (Howe 1998), but also allows an extension to other geometries, such as a tilted cylindrical perforation for instance. As in Rayleigh's (Rayleigh 1945) and Howe's (Howe 1998) methods, the main ingredient is a variational theory linked to minimization of kinetic energy, but here both the dual Dirichlet and Kelvin variational principles come into play. This theory arises in Lagrangian and Hamiltonian mechanics and is of great importance in several fields, especially in mathematical modelling (Courant & Hilbert 1953, Chap 4, Sect 9) to obtain lower and upper bounds for potential and kinetic energies, in optimization (Luenberger 1997) to derive the dual formulations, and in numerical analysis (Roberts & Thomas 1991, Chap 1) for assessing the validity or the accuracy of a numerical solution. Laurens *et al.* (2012) derived a rigorous mathematical framework for applying this theory to the thick perforated plate configuration. Here, the main points of this theoretical work are summarized, without giving details of the mathematical proofs. Our focus is rather on the results obtained for several geometrical configurations including in particular the case of elliptical apertures which were not covered in Laurens *et al.* (2012).

3.1. *A brief description of the theory*

First of all, the boundary-value problem (2.9) is converted in a more condensed form through the change of variable $p' = \left(p - (P^+ + P^-)/2\right) / \left(P^+ - P^-\right)$. For simplicity, in

what follows the prime will be removed. This yields:

$$\begin{cases} \nabla^2 p = 0 & \text{in } \mathsf{U} \\ \partial_{\boldsymbol{n}} p = 0 & \text{on the walls} \\ p^{\pm} = \lim_{x_3 \to \pm\infty} p = \pm\, 1/2 & \text{on } \mathsf{U}_{\pm}. \end{cases} \tag{3.1}$$

The Rayleigh conductivity (2.11) can now be defined as:

$$K_R = \int_{D_+} \partial_{x_3} p \, \mathrm{d}\boldsymbol{x}'. \tag{3.2}$$

Consider the functional

$$\mathsf{J}(\psi, \boldsymbol{q}) = \int_U \left| \boldsymbol{q}(\boldsymbol{x}) - \boldsymbol{\nabla}\psi(\boldsymbol{x}) \right|^2 \, \mathrm{d}\boldsymbol{x}, \tag{3.3}$$

where $(\psi, \boldsymbol{q})$ run over adequate spaces of functions $\mathsf{H}_{1/2}(\mathsf{U})$ and $\mathsf{W}(\mathsf{U})$, where $\mathsf{H}_{1/2}(\mathsf{U})$ is the space of functions ψ so that $\boldsymbol{\nabla}\psi$ is square integrable in U and with traces at infinity $\psi^{\pm} = \pm 1/2$, and $\mathsf{W}(\mathsf{U})$ is the space of square integrable vectorial functions $\boldsymbol{q}$ so that $\boldsymbol{\nabla} \cdot \boldsymbol{q} = 0$ in U and $\boldsymbol{q} \cdot \boldsymbol{n} = 0$ on the boundary of U. The functional $\mathsf{J}(\psi, \boldsymbol{q})$ can also be written in the form:

$$\mathsf{J}(\psi, \boldsymbol{q}) = \int_{\mathsf{U}} |\boldsymbol{q}(\boldsymbol{x})|^2 \, \mathrm{d}\boldsymbol{x} + \int_{\mathsf{U}} |\boldsymbol{\nabla}\psi(\boldsymbol{x})|^2 \, \mathrm{d}\boldsymbol{x} - 2 \int_{\mathsf{U}} \boldsymbol{\nabla}\psi \cdot \boldsymbol{q}(\boldsymbol{x}) \, \mathrm{d}\boldsymbol{x} \tag{3.4}$$

Laurens *et al.* (2012) proved that the following relation holds, thanks to the properties of the spaces of functions $\mathsf{H}_{1/2}(\mathsf{U})$ and $\mathsf{W}(\mathsf{U})$:

$$\int_{\mathsf{U}} \boldsymbol{\nabla}\psi \cdot \boldsymbol{q}(\boldsymbol{x}) \, \mathrm{d}\boldsymbol{x} = \int_{D^+} \boldsymbol{q}_3 \, \mathrm{d}\boldsymbol{x}' = \int_{D^-} \boldsymbol{q}_3 \, \mathrm{d}\boldsymbol{x}'. \tag{3.5}$$

Thus, J can be decomposed into $\mathsf{J}(\psi, \boldsymbol{q}) = \mathsf{J}_1(\psi) - \mathsf{J}_2(\boldsymbol{q})$ with

$$\mathsf{J}_1(\psi) = \int_{\mathsf{U}} \left| \boldsymbol{\nabla}\psi(\boldsymbol{x}) \right|^2 \mathrm{d}\boldsymbol{x} \text{ and } \mathsf{J}_2(\boldsymbol{q}) = 2 \int_{D_+} \boldsymbol{q}_3(\boldsymbol{x}) \, \mathrm{d}\boldsymbol{x}' - \int_{\mathsf{U}} |\boldsymbol{q}(\boldsymbol{x})|^2 \, \mathrm{d}\boldsymbol{x}. \tag{3.6}$$

The Kelvin and Dirichlet principles are based on performing this decomposition and considering the dual expressions for the energy $\mathsf{J}_1(\psi)$ and $\mathsf{J}_2(\boldsymbol{q})$.
Obviously, as p is the solution to system (3.1), it belongs to $\mathsf{H}_{1/2}(\mathsf{U})$, $\boldsymbol{\nabla}p$ belongs to $\mathsf{W}(\mathsf{U})$ and $\mathsf{J}(p, \boldsymbol{\nabla}p) = 0$. Moreover, equations (3.2) and (3.5) show easily that $\mathsf{J}_1(p) = K_R$, which directly leads to $K_R = \mathsf{J}_1(p) = \mathsf{J}_2(\boldsymbol{\nabla}p)$. It can then be established (see Laurens *et al.* 2012) that J_1 reaches its unique minimum at p and J_2 its unique maximum at $\boldsymbol{\nabla}p$, which leads to the following lemma.

LEMMA 1. *The Rayleigh conductivity K_R can be obtained equivalently in one of the following forms:*

$$\begin{cases} \textbf{\textit{Dirichlet principle:}} & K_R = \min_{\psi \in \mathsf{H}_{1/2}} \mathsf{J}_1(\psi) \\ & \quad \textit{with } \mathsf{J}_1(\psi) = \displaystyle\int_{\mathsf{U}} \left| \boldsymbol{\nabla}\psi(\boldsymbol{x}) \right|^2 \mathrm{d}\boldsymbol{x} \\ \textbf{\textit{Kelvin principle:}} & K_R = \max_{\boldsymbol{q} \in \mathsf{W}} \mathsf{J}_2(\boldsymbol{q}) \\ & \quad \textit{with } \mathsf{J}_2(\boldsymbol{q}) = 2 \displaystyle\int_{D^+} \boldsymbol{q}_3(\boldsymbol{x}) \, \mathrm{d}\boldsymbol{x}' - \int_{\mathsf{U}} |\boldsymbol{q}(\boldsymbol{x})|^2 \, \mathrm{d}\boldsymbol{x}. \end{cases} \tag{3.7}$$

This lemma shows that lower and upper bounds for the Rayleigh conductivity can be obtained for any arbitrary geometry of the perforation, provided that the spaces $\mathsf{H}_{1/2}$ and W can be expressed accurately enough and the functionals $\mathsf{J}_1(\psi)$ and $\mathsf{J}_2(\boldsymbol{q})$ explicitly

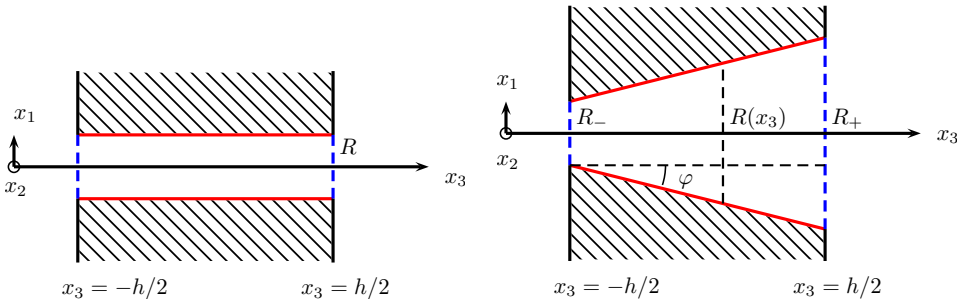

(a) Cylindrical aperture of radius R

(b) Conical aperture of radius $R(x_3)$, with $0 \leqslant \varphi < \pi/2$

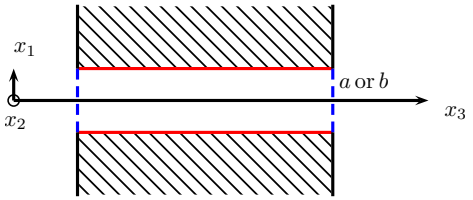

(c) Elliptical aperture with major radius a and minor radius b

Figure 3: Geometries of untilted perforations

evaluated. In Laurens *et al.* (2012), the Rayleigh conductivity is calculated for the case of untilted cylindrical and conical apertures, as well as for a tilted cylindrical perforation. In what follows, results for the Rayleigh conductivity bounds are reviewed without giving all the mathematical steps, and are expressed in terms of end corrections. Additional cases of untilted and tilted apertures with an elliptical section are also addressed. Detailed expressions of functions ψ and $\boldsymbol{q}$ used to obtain bounds for the Rayleigh conductivity for each geometry are given in appendix A.

3.2. *Untilted perforations*

In this section, various geometries are considered. They are displayed in figure 3 and denoted as *untilted* apertures since their axis of symmetry is perpendicular to the plate surface.

3.2.1. *Circular hole*

The case of a circular hole (see figure 3a) was already addressed by Howe (1998). He established the following bounds for the Rayleigh conductivity:

$$\frac{\pi R^2}{h + 16R\,/\,3\pi} \leqslant K_{R,\mathrm{cyl}} \leqslant \frac{\pi R^2}{h + \pi R/2}. \tag{3.8}$$

Identical values to Howe's ones are obtained using lemma 1. It is instructive to express these relations in terms of the length $l = s/K_R$, where s is the area of the aperture. This length can be interpreted as the effective length of a slug of fluid of cross section s involved in the motion through the aperture. The conductivity of the channel alone is $\pi R^2/h$, for which l would be h. Thus, equation (3.8) can be expressed in terms of an end correction l', defined by $l = h + l'$, so that l' is the amount by which h must be increased to account for the contributions of the openings. The end correction for the cylindrical

case is therefore:

$$\frac{\pi R}{2} \leqslant l'_{\rm cyl} \leqslant \frac{16R}{3\pi}. \tag{3.9}$$

It should be noted that this end correction can be directly linked to the specific acoustic impedance of the perforation, defined in the notation of section 2 as:

$$z = \frac{1}{\rho_0 c_0} \frac{P^+ - P^-}{-v_3} \tag{3.10}$$

As proposed by Jing & Sun (2000), the impedance can indeed be decomposed into the impedance induced by the end correction $z_e = -\mathrm{i}\kappa l'$ and the added inertial term $-\mathrm{i}\kappa h$:

$$z = z_e - \mathrm{i}\kappa h = -\mathrm{i}\kappa(l' + h) \tag{3.11}$$

3.2.2. *Conical hole*

In industrial applications, perforated plates are often manufactured by laser drilling. There may also be tapered holes see Yu *et al.* (1999), chapter 4, for instance, as holes on the drilled entry side are larger than those on the drilled exit side. This kind of hole can be characterized as a conical perforation defined by:

$$\Omega = \left\{ \boldsymbol{x} \in \mathbb{R}^3 \mid (x_1, x_2) \in \mathsf{D}_{R(x_3)} \text{ and } -h/2 \leqslant x_3 \leqslant h/2 \right\} \tag{3.12}$$

where $\mathsf{D}_{R(x_3)}$ is the disc of radius $R(x_3)$ that varies linearly from R_- to R_+ (see figure 3b). Lemma 1 gives:

$$\frac{\pi R_- R_+}{h + \frac{8}{3\pi}\Big(R_+ + R_-\Big) + \frac{1}{2h}\Big(R_+ - R_-\Big)^2} \leqslant K_{R,\rm con} \leqslant \frac{\pi R_- R_+}{h + \frac{\pi}{4}\Big(R_+ + R_-\Big)}. \tag{3.13}$$

The bounds (3.13) have to be compared with Howe's estimates (Howe 1998, p.359). There is a missed factor 2 in the last term in the denominator of the lower bound for Howe's estimate, apparently a typing error.
These expressions for the Rayleigh conductivity show that, as in the cylindrical case, the plate thickness h can be corrected. Bounds for the end correction corresponding to an effective section $s = \pi R_- R_+$ can be stated as follows:

$$\frac{\pi}{4}\Big(R_+ + R_-\Big) \leqslant l'_{\rm con} \leqslant \frac{8}{3\pi}\Big(R_+ + R_-\Big) + \frac{1}{2h}\Big(R_+ - R_-\Big)^2. \tag{3.14}$$

3.2.3. *Hole with an elliptical aperture*

The semi-major and semi-minor axes of the elliptical aperture are respectively a and b while the thickness of the plate is once again assumed to be h (see figure 3c):

$$\Omega = \left\{ \boldsymbol{x} \in \mathbb{R}^3 \;\middle|\; \frac{x_1^2}{a^2} + \frac{x_2^2}{b^2} < 1 \text{ with } a > b \text{ and } -\frac{h}{2} < x_3 < \frac{h}{2} \right\}. \tag{3.15}$$

Applying lemma 1 leads to:

$$\frac{\pi ab}{h + \frac{16b}{3\pi}\frac{K(\varepsilon)}{K(0)}} \leqslant K_{R,\rm ell} \leqslant \frac{\pi ab}{h + \frac{\pi b}{2}\frac{K(\varepsilon)}{K(0)}}, \tag{3.16}$$

with $\varepsilon = \sqrt{1 - b^2/a^2}$ the eccentricity of the ellipse and $K(\varepsilon)$ the complete elliptic integral of the first kind defined by:

$$K(\varepsilon) = \int_0^{\pi/2} \left(1 - \varepsilon^2 \sin^2\phi\right)^{-1/2} \mathrm{d}\phi. \tag{3.17}$$

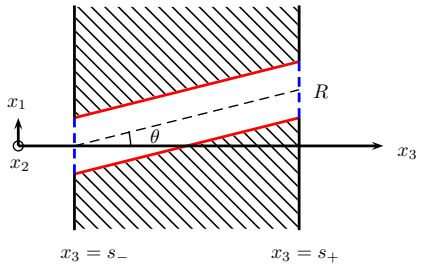

Figure 4: Aperture tilted at an angle θ to the x_3 axis. The cross section can be either a disc of radius R or an ellipse of major and minor axis (a, b) and $-\pi/2 < \theta < \pi/2$.

As explained by Morfey (1969), the upper bound of equation (3.16) was found by Lord Rayleigh (Rayleigh 1945, chapter 1, section 304) for an infinitely thin plate ($h = 0$). The lower bound expression is, to the best of the authors' knowledge, entirely new. The results of the present study can once again be expressed in terms of an end correction. With an effective section $s = \pi ab$, the bounds for this end correction are:

$$\frac{\pi b}{2}\frac{K(\varepsilon)}{K(0)} \leqslant l'_{\text{ell}} \leqslant \frac{16b}{3\pi}\frac{K(\varepsilon)}{K(0)}. \tag{3.18}$$

3.3. *Tilted perforations*

In cooling liners used in combustion chambers, apertures are not perpendicular to the plate, but are tilted at an angle to the x_3 axis that is often around 60°(see Eldredge *et al.* 2007; Andreini *et al.* 2011). A diagram of this kind of geometry is shown in figure 4. Kelvin and Dirichlet principles are now used to derive bounds for the Rayleigh conductivity of these configurations, and in particular, an estimate for the end correction for such tilted geometries.

3.3.1. *Tilted perforation with a circular section*

A cylindrical perforation with a θ tilting angle can be described as follows:

$$\Omega = \Big\{ \boldsymbol{x} \in \mathbb{R}^3 \mid (\widehat{x}_1(\boldsymbol{x}), x_2) \in \mathsf{D}_R \text{ and } -h/2 < x_3 < h/2 \Big\}, \tag{3.19}$$

with

$$\widehat{x}_1(\boldsymbol{x}) = x_1 - (x_3 + h/2)\,\tan\theta, \tag{3.20}$$

and $-\pi/2 < \theta < \pi/2$. The perforation is chosen so that it cuts any plane parallel to the plate along a circle of radius R. Lemma 1 directly yields the following bounds of the Rayleigh conductivity.

$$\frac{\pi R^2}{\frac{h}{\cos^2\theta} + \frac{16R}{3\pi}} \leqslant K_{R,\text{tilted}} \leqslant \frac{\pi R^2}{\frac{h}{\cos^2\theta}\Big/\Big(1 + \frac{16R}{3\pi h}\sin^2\theta\Big) + \frac{\pi R}{2}}. \tag{3.21}$$

As expected, the untilted cylinder bounds (3.8) are recovered when $\theta = 0$. Moreover, equation (3.21) shows that the tilting angle has a non-intuitive influence on the Rayleigh conductivity of the perforation. Indeed, the bounds for the effective length of fluid motion associated with section $s = \pi R^2$ are given by:

$$\frac{h}{\cos^2\theta}\Big/\left(1 + \frac{16R}{3\pi h}\sin^2\theta\right) + \frac{\pi R}{2} \leqslant l_{R,\text{tilted}} \leqslant \frac{h}{\cos^2\theta} + \frac{16R}{3\pi}. \tag{3.22}$$

This length can be decomposed into an end correction l' and an effective height $\widetilde{h}$ such that:

$$l = \widetilde{h} + l' = \frac{h}{\cos^2\theta} + l'. \tag{3.23}$$

The effective height $\widetilde{h}$ is hence quite different from the intuitive effective thickness of the perforation $h/\cos\theta$ that has been found until now in the literature (Andreini *et al.* 2011; Mendez & Eldredge 2009; Eldredge *et al.* 2007). Applying Kelvin and Dirichlet principles in a rigorous way has thus led to a result that could not be obtained heuristically. Finally equation (3.21) gives the following bounds for the end correction:

$$f(h) + \frac{\pi R}{2} \leqslant l'_{R,\mathrm{inc}} \leqslant \frac{16R}{3\pi}, \tag{3.24}$$

with $f(h) = -\frac{16R}{3\pi}\tan^2\theta \,/\big(1 + \frac{16R}{3\pi h}\sin^2\theta\big) \leqslant 0$.

3.3.2. *Tilted perforation with an elliptical section*

The general case of a tilted perforation with an elliptical cross-section is now addressed. This case is more realistic, since it is representative of genuine perforations. Indeed, when a drill bit of radius R is used for boring holes tilted by θ degrees from the vertical, it results in a perforation which cuts any parallel plane to the plate along an ellipse of major axis (in the tilt direction) $2a = 2R/\cos\theta$ and minor axis (in the transversal direction) $2b = 2R$. We then get:

$$\Omega = \left\{ \boldsymbol{x} \in \mathbb{R}^3 \;\middle|\; \frac{\widehat{x}_1^2}{a^2} + \frac{x_2^2}{b^2} < 1 \;\text{ with } a > b \text{ and } -\frac{h}{2} < x_3 < \frac{h}{2} \right\}, \tag{3.25}$$

with $\widehat{x}_1^2$ defined as in (3.20). Kelvin and Dirichlet principles then give the following bounds for the Rayleigh conductivity:

$$\frac{\pi ab}{\frac{h}{\cos^2\theta} + \frac{16b}{3\pi}\frac{K(\varepsilon)}{K(0)}} \leqslant K_{R,\mathrm{ell,inc}} \leqslant \frac{\pi ab}{\frac{\pi b}{2}\frac{K(\varepsilon)}{K(0)} + \frac{h}{\cos^2\theta}\Big/\Big(1 + \frac{16a^2}{3\pi bh}\frac{D(0)}{D(\varepsilon)}\sin^2\theta\Big)}, \tag{3.26}$$

with $D(0) = \pi/4$ and

$$D(\varepsilon) = \int_0^{\pi/2} \frac{\sin^2\phi}{\sqrt{1 - \varepsilon^2\sin^2\phi}}\, d\phi = \frac{K(\varepsilon) - E(\varepsilon)}{\varepsilon^2}, \tag{3.27}$$

where $E(\varepsilon)$ is the complete elliptic integral of the second kind:

$$E(\varepsilon) = \int_0^{\pi/2} \big(1 - \varepsilon^2\sin^2\phi\big)^{1/2}\; \mathrm{d}\phi. \tag{3.28}$$

For $a = b/\cos\theta$, expression (3.26) becomes simpler

$$\frac{\pi ab}{\frac{h}{\cos^2\theta} + \frac{16b}{3\pi}\frac{K(\varepsilon)}{K(0)}} \leqslant K_{R,\mathrm{ell,inc}} \leqslant \frac{\pi ab}{\frac{\pi b}{2}\frac{K(\varepsilon)}{K(0)} + \frac{h}{\cos^2\theta}\Big/\Big(1 + \frac{16b}{3\pi h}\frac{D(0)}{D(\varepsilon)}\tan^2\theta\Big)}. \tag{3.29}$$

Once again, these results show that the modified effective height $\widetilde{h} = h/\cos^2\theta$ is the most relevant parameter. The end correction, defined by considering the effective section $s = \pi ab$ can be bounded as follows:

$$\frac{\pi b}{2}\frac{K(\varepsilon)}{K(0)} + g(h) \leqslant l'_{\mathrm{ell,inc}} \leqslant \frac{16b}{3\pi}\frac{K(\varepsilon)}{K(0)}, \tag{3.30}$$

with $g(h) = -\frac{16b}{3\pi}\frac{D(0)}{D(\varepsilon)} \Big/ \left(\sin^2\theta + \frac{16b}{3\pi}\frac{D(0)}{D(\varepsilon)}\frac{\cos^2\theta}{h}\right) \leqslant 0$. As expected, setting $\theta = 0$ yields the untilted elliptical aperture case (3.18) if the eccentricity ε is kept constant, or the untilted cylindrical case (3.9) if the perforation remains circular.

However, since for this specific geometry we have $\pi ab = \pi R^2/\cos\theta$, the bounds (3.26) for the Rayleigh conductivity can also be expressed as follows:

$$\frac{\pi R^2}{\frac{h}{\cos\theta} + \frac{16R}{3\pi}\frac{K(\varepsilon)}{K(0)}\cos\theta} \leqslant K_{R,\mathrm{ell,inc}} \leqslant \frac{\pi R^2}{\frac{\pi R}{2}\frac{K(\varepsilon)}{K(0)}\cos\theta + \frac{h}{\cos\theta}\Big/\left(1 + \frac{16R}{3\pi h}\frac{D(0)}{D(\varepsilon)}\tan^2\theta\right)}, \tag{3.31}$$

Then, if we consider the section along the tilted axis $x_3\cos\theta$ (which is circular with an area πR^2), as the reference section instead of the effective section $\pi ab = \pi R^2/\cos\theta$, Eq. (3.31) shows that the effective height, which then has to be considered, is $h/\cos\theta$ instead of $h/\cos^2\theta$ as in (3.26). Other pairs (section, height) can be considered, but the previous two, i.e., $(\pi ab, h/\cos^2\theta)$ and $(\pi R^2, h/\cos\theta)$, are the most natural ones.

3.4. *Numerical results*

In this section, the influence of the geometry on the Rayleigh conductivities and end corrections is numerically investigated for some generic configurations.

3.4.1. *Generic perforated plate*

The multiperforated plate under consideration is among those typically involved in combustion chambers. Such plates have quite a low porosity ($\approx 2\%$). Consequently the individual apertures can be assumed to be coupled only through long range interactions which means that the results of sections 3.2 and 3.3 apply. The plate thickness is $h = 2$mm and the characteristic size of the perforations is $r = 0.225$mm. This length will be the radius R of the section of a circular perforation, the small radius R_- of the conical perforations, and the semi-minor axis b of the section of the elliptical perforations.

The reference values for the Rayleigh conductivity and the end correction will be respectively the upper and lower bounds of these parameters, corresponding to a untilted cylindrical hole:

$$K_R^{\mathrm{ref}} = \frac{\pi r^2}{h + \pi r/2}, \quad l_{\mathrm{ref}} = \pi r/2 \tag{3.32}$$

In particular, we have $h = 5.66\, l_{\mathrm{ref}}$.

The results for the untilted perforations are plotted in figures 5 and 6, for the end corrections and Rayleigh conductivities respectively. Figure 5 shows that significant deviations from the cylindrical case are obtained for the end correction, even for small angles of the conical aperture or a small elongation of the elliptical section.

These variations are large enough to imply a significant change on the Rayleigh conductivity (see figure 6), even when the plate thickness h is much larger than the size of the apertures.

For tilted circular or elliptical apertures, it has been previously shown that the plate thickness has to be taken into account in a non-intuitive way, by considering an effective thickness of $h/\cos^2\theta$ rather than the length of the centerline of the tilted aperture $h/\cos\theta$. Differences between these two expressions are shown in figure 7 for a tilting angle varying from 0 to the conventional 60° value. It is worth noting that for large tilting angles the inertial contribution $\widetilde{h}$ is much greater than for the untilted case.

End corrections and Rayleigh conductivities are plotted in figures 8 and 9, respectively. Major variations occur when the tilting angle is increased. A divergence between lower and upper bounds of the end corrections is observed for large values of these angles.

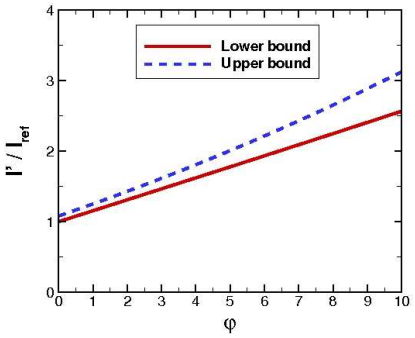

(a) Scaled end correction versus the angle of the conical aperture in degrees

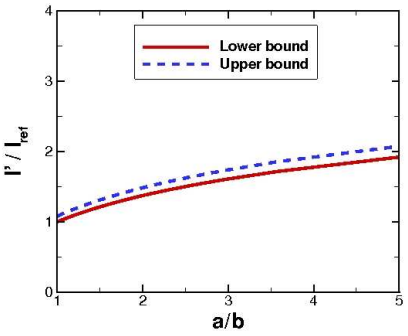

(b) Scaled end correction versus the ratio of the semi-major to the semi-minor axis of the ellipse

Figure 5: Scaled end corrections for the conical and elliptical untilted apertures.

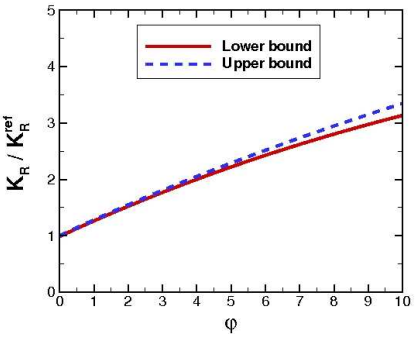

(a) Scaled Rayleigh conductivity versus the angle of the conical aperture, in degrees

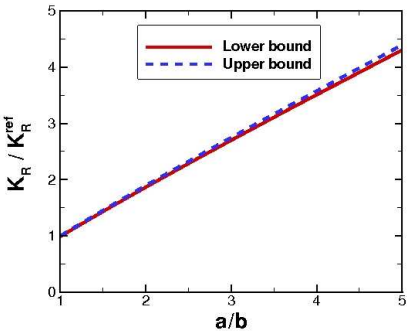

(b) Scaled Rayleigh conductivity versus the ratio between the major and minor radii of the ellipse

Figure 6: Scaled Rayleigh conductivities for the conical and elliptical untilted apertures.

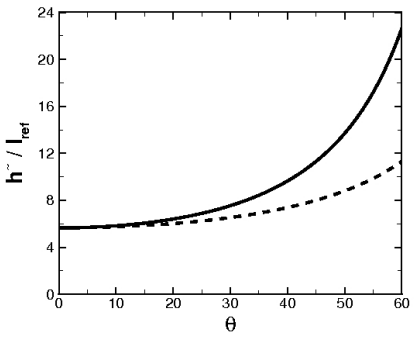

Figure 7: Scaled effective thickness $\tilde{h}$. Correct expression $\tilde{h} = h/\cos^2\theta$ in solid line, intuitive expression $\tilde{h} = h/\cos\theta$ in dashed line. The tilting angle θ is in degrees.

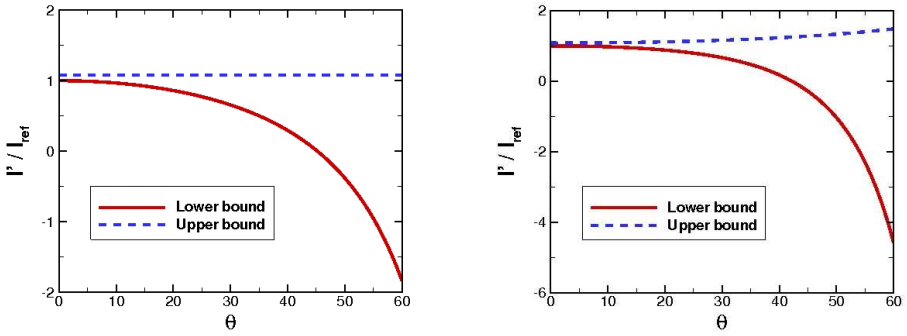

(a) Cylindrical aperture (b) Elliptical aperture

Figure 8: Scaled end corrections for the cylindrical and elliptical tilted apertures. The tilting angle θ is in degrees.

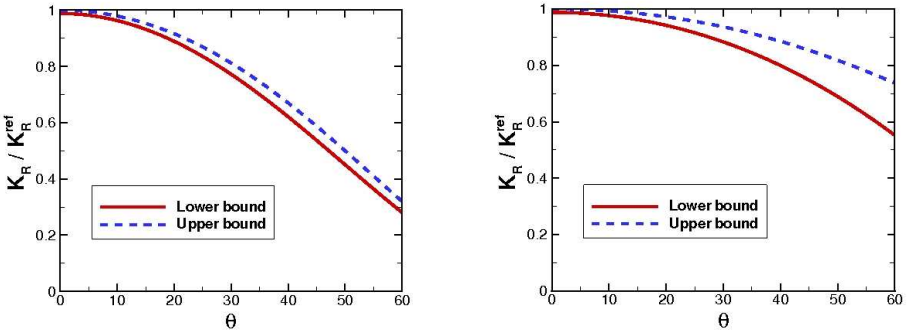

(a) Cylindrical aperture (b) Elliptical aperture

Figure 9: Scaled Rayleigh conductivities for the cylindrical and elliptical tilted apertures. The tilting angle θ is in degrees.

However, this is mostly due to the fast increase of $\widetilde{h}$ which plays a prominent role in this case. Indeed, figure 9 shows that the lower and upper bounds of the Rayleigh conductivitiy do not differ significantly.

All these results show that geometrical features greatly affect the Rayleigh conductivities or end corrections of apertures, and thus cannot be discarded if the effects of this parameter on the acoustic properties of the plate are to be taken into account accurately. Of course, this is only true if the potential component of the plate impedance is significant, which is not the case for liners in grazing flow ducts, for instance. However, the potential form of the Rayleigh conductivity is the basis for models used in bias flow configurations, and an accurate description of it can be of great help, as will be shown in the next section.

3.4.2. *Eldredge et al. numerical simulations*

The influence of the geometrical features can also be illustrated from the numerical simulations of Eldredge *et al.* (2007) who performed incompressible large-eddy simulations of the acoustic response of a turbulent flow through a multiperforated liner. The apertures had a circular bore of diameter $2R = 5$mm, a tilting angle $\theta = 60^o$, and a

	Tilted cylinder	Tilted ellipse	Eldredge *et al.* expression with $l = h/\cos\theta$	Eldredge *et al.* expression with $l = 0.75h/\cos\theta$
K_R^-	$4.44\,10^{-4}$	$8.57\,10^{-4}$	$8.21\,10^{-4}$	$10.00\,10^{-4}$
K_R^+	$5.73\,10^{-4}$	$14.18\,10^{-4}$		

Table 1: Bounds of the Rayleigh conductivity obtained from expressions established in section 3.3, compared with the values used in the paper by Eldredge *et al.* .

thickness $h = 10$mm. Thus, at the bottom and top of the plate, the holes were elliptical with a major axis of 10mm and a minor axis of 5mm. However, the cross section along the tilted axis was circular with a cross-section of πR^2. This case corresponds exactly to the configuration studied in section 3.3.2.

We recall that, for this configuration, if the reference section is chosen to be πR^2, the effective length to be considered is $h/\cos\theta$. This is the value used by Eldredge *et al.* for calculating the Rayleigh conductivity of the hole, but they applied it with a modified version of Howe's model in which the no-flow Rayleigh conductivity was in fact the upper bound of the untilted cylinder bounds (3.8). The model is somewhat close to the simulation results, but the authors obtained a better agreement by taking the effective height to be $l = 0.75h/\cos\theta$. They explained that this decrease of the effective l may be due to the fact that the radius of the aperture is effectively larger than R because of the elliptical intersection of the aperture with the top and bottom of the plate.

Table 1 summarizes the values of the no-flow Rayleigh conductivity proposed by Eldredge *et al.* and the analytical bounds obtained using the expressions established in section 3.3. The Eldredge *et al.* value obtained with $l = 0.75h/\cos\theta$ fits perfectly between the bounds for the tilted ellipse given by (3.31), and is quite close to the mean value of the bounds $K_R = (K_R^- + K_R^+)/2 = 11,375.10^{-4}$. On the contrary, their first value obtained with $l = h/\cos\theta$, is lower than the lower bound for a tilted ellipse and greater than the upper bound for a tilted cylinder of radius R given by (3.21). This points out the importance of the tilted angle in the computation of the Rayleigh conductivity. The coefficient 0.75 introduced by Eldredge *et al.* corrects empirically the difference between the bounds for a untilted cylinder (3.8) and for a tilted aperture with elliptical section (3.31). The bounds (in 3.31) therefore yield an increased accuracy of the Rayleigh conductivity approximation, by taking into account the dependency on the parameters a and b of the ellipse, as well as on the tilted angle θ.

These results confirm that taking the geometry of the aperture into account correctly is advantageous. Of course, the question of the modification of the no-flow Rayleigh conductivity in the presence of a bias flow is still open. Strategies used until now, which consist in modifying this value by a flow dependent function (either as did by Jing & Sun (2000) or in a slightly different way by Luong *et al.* (2005)) may still be relevant.

4. Effective acoustic compliance of a low-porosity perforated plate

In this section, we introduce a method for determining the reflection and transmission coefficients of a low-porosity perforated plate.

It is an adaptation of an approach previously used by Leppington & Levine (1973) for dealing with thin perforated plates. Actually, the method devised by Leppington and Levine is extended here in several directions. The plate is no longer assumed to be thin and the perforations can be of a rather arbitrary shape. Since the procedure is in fact a

method for approximating the reflected and transmitted waves, the order of the approximation is specified thus making it possible to derive second-order asymptotic expansions of the acoustic wave. As mentioned above, it is worth recalling that the perforated plates under consideration in this study are of low-porosity so that a characteristic size d of a perforation can be assumed to be negligible when compared with the spacing L between two neighboring perforations as well as the acoustic wavelength.

The analytical expressions obtained rely upon the Rayleigh conductivity as a key parameter. The main mathematical tools are asymptotic expansions, integral equations, and the lattice sum theory for the Helmholtz equation (Linton 2010). The reflection and transmission coefficients are moreover used to derive an effective compliance for the plate.

4.1. *Scattering problem and Floquet's modes*

Consider the configuration shown in figure 1a of an acoustic plane wave incident upon a perforated plate. As is well-known in lattice theory (see, e.g., Nedelec & Starling (1991), Linton (2010)), the total wave satisfies the following quasi-periodic conditions resulting from the periodicity properties of the array and the fact that translating the incident wave by a vector $\boldsymbol{\xi}_m$, linked to the periodicity properties of the lattice (see (2.5)), simply shifts the phase according to the following formula

$$p(\boldsymbol{x}+\boldsymbol{\xi}_m) = e^{\mathrm{i}\boldsymbol{\beta}\cdot\boldsymbol{\xi}_m} p(\boldsymbol{x}), \tag{4.1}$$

where $\boldsymbol{\beta}\cdot\boldsymbol{\xi}_m$ is the scalar product of the Bloch vector $\boldsymbol{\beta} = \kappa\boldsymbol{\tau}'$ and $\boldsymbol{\xi}_m$. In the following, when saying that p satisfies periodic boundary conditions, we mean that p, as well as any of its derivatives, satisfies (4.1). It is therefore sufficient to restrict the determination of the wave p to the unit cell displayed in figure 2.

This determination requires a radiation condition on the reflected wave $\left(p - p_i\right)|_{\mathsf{U}_+}$ and the transmitted one $p|_{\mathsf{U}-}$, which can be set in terms of a series of Floquet modes (see Bendali *et al.* 2012; Linton 2010; Nedelec & Starling 1991, for instance).

As a result, the wave reflected and transmitted by the multiperforated plate can be specified in the unit cell by solving the following boundary-value problem:

$$\begin{cases} \nabla^2 p + \kappa^2 p = 0 & \text{in } \mathsf{U} \\ \partial_{\boldsymbol{n}} p = 0 & \text{on the plate,} \end{cases} \tag{4.2}$$

together with outgoing radiation conditions and periodicity properties (4.1) on the fictitious boundaries $\partial\mathsf{U}_\pm$, for p and its derivatives.

4.2. *A domain decomposition approach*

A boundary integral equation formulation is used on $\mathsf{U}_\pm$. In the following, for the sake of clarity, the plate is assumed to be located between $x_3 = -h/2$ and $x_3 = h/2$.

In Leppington & Levine (1973), the main tool for dealing with the wave outside the perforations is the quasi-periodic Green's kernel for the Helmholtz equation G_Λ:

$$G_\Lambda(\boldsymbol{x},\boldsymbol{y}) = \sum_m e^{\mathrm{i}\boldsymbol{\beta}\cdot\boldsymbol{\xi}_m} G((\boldsymbol{x}'-\boldsymbol{y}', |x_3|), \boldsymbol{\xi}_m), \tag{4.3}$$

with $\boldsymbol{x} = (\boldsymbol{x}', x_3)$, $\boldsymbol{y} = (\boldsymbol{y}', 0)$. The underlying kernel

$$G(\boldsymbol{x},\boldsymbol{\xi}) = \frac{e^{\mathrm{i}\kappa|\boldsymbol{x}-\boldsymbol{\xi}|}}{4\pi|\boldsymbol{x}-\boldsymbol{\xi}|}, \tag{4.4}$$

is the standard Green one yielding the outgoing solution to the Helmholtz equation. The solution of the scattering problem when the plate is considered as perfectly reflecting can

be explicitely written as:

$$\begin{cases} p_0(\boldsymbol{x}) = p_i\left(\boldsymbol{x}', x_3\right) + p_i\left(\boldsymbol{x}', -x_3\right) & \text{for } x_3 \geqslant h/2 \\ p_0(\boldsymbol{x}) = 0 & \text{for } x_3 \leqslant -h/2. \end{cases} \tag{4.5}$$

Then, the solution to the boundary-value problem posed in the previous section can be expressed, outside the perforation, in terms of a single integral equation written in local coordinates:

$$p_\pm(\boldsymbol{x}_\pm) = p_0(\boldsymbol{x}_\pm) \mp \int_{\mathsf{D}_\pm} 2\, G_\Lambda(\boldsymbol{x}_\pm, \boldsymbol{y}) \partial_{x_3} p_+(\boldsymbol{y}', 0) \mathrm{d}\boldsymbol{y}' \tag{4.6}$$

Indeed, the quasi-periodic Green kernel G_Λ takes into account all the following features: the Helmholtz equation, the quasi-periodic conditions and the outgoing radiation conditions. The acoustic pressure within the hole can hence be obtained by solving the following system:

$$\begin{cases} \nabla^2 p + \kappa^2 p = 0 & \text{on } \Omega \\ \partial_{\boldsymbol{n}} p = 0 & \text{on } \Sigma \\ p_\pm(\boldsymbol{x}_\pm) = p_0(\boldsymbol{x}_\pm) \mp \displaystyle\int_{\mathsf{D}_\pm} 2\, G_\Lambda(\boldsymbol{x}_\pm, \boldsymbol{y}) \partial_{x_3} p_+(\boldsymbol{y}', 0) \mathrm{d}\boldsymbol{y}'. \end{cases} \tag{4.7}$$

combined with transmission conditions between the hole and the integral formulation within the upper and lower cells:

$$\begin{cases} p = p_+ \text{ on } \mathsf{D}_+, \\ p = p_- \text{ on } \mathsf{D}_-, \end{cases} \qquad \text{and} \qquad \begin{cases} \partial_{x_3} p = \partial_{x_3} p_+ \text{ on } \mathsf{D}_+, \\ \partial_{x_3} p = \partial_{x_3} p_- \text{ on } \mathsf{D}_-. \end{cases} \tag{4.8}$$

It is worth noting that the above transmission conditions are expressed in terms of functions defined on the same sets instead of functions depending on the same variables. It is in this context that the domain decomposition approach can handle efficiently the incident and reflected waves on one hand and the transmitted wave on the other hand.

4.3. *Second-order asymptotic expansions*

As mentionned previously (see (2.6)), the wavelength λ is always assumed to satisfy $L < \lambda/2$. As a result, the condition that the characteristic size of the perforation d is negligible relative to the space between two successive perforations and to the wavelength λ can be more conveniently expressed by means of the dimensionless parameter $\delta = d/L \ll 1$. It should be noted that this is simply a consequence of assuming that the plate has a low porosity. Dual, or spectral, representations of the Green's kernel G_Λ for $|x_3| \gg 1$ (see, e.g. Linton 2010, formula (2.9)) make it possible to obtain the reflection and the transmission coefficients, respectively denoted R_δ and T_δ to underline their dependence on δ, through the following decomposition of the wave in a propagative and an evanescent part:

$$\begin{aligned} p(\boldsymbol{x}'_+, x_3^+) &= e^{\mathrm{i}\kappa \boldsymbol{\tau}'\cdot\boldsymbol{x}'_+} \left(e^{-\mathrm{i}\kappa\cos\Phi x_3^+} + R_\delta e^{\mathrm{i}\kappa\cos\Phi x_3^+} \right) + \text{evan. modes} && \text{for } x_3^+ > 0, \\ p(\boldsymbol{x}'_-, x_3^-) &= e^{\mathrm{i}\kappa \boldsymbol{\tau}'\cdot\boldsymbol{x}'_-} \, T_\delta e^{-\mathrm{i}\kappa\cos\Phi x_3^-} + \text{evan. modes} && \text{for } x_3^- < 0, \end{aligned} \tag{4.9}$$

with

$$\begin{cases} R_\delta = 1 - \displaystyle\int_{\mathsf{D}_+} 2 G_\Lambda(\boldsymbol{x}_+, \boldsymbol{y}) \partial_{x_3} p_+(\boldsymbol{y}', 0) \mathrm{d}\boldsymbol{y}' \\ T_\delta = \displaystyle\int_{\mathsf{D}_-} 2 G_\Lambda(\boldsymbol{x}_-, \boldsymbol{y}) \partial_{x_3} p_-(\boldsymbol{y}', 0) \mathrm{d}\boldsymbol{y}' \end{cases} \tag{4.10}$$

A Poisson summation formula is used to express the quasi-periodic Green's kernel in terms of propagative and evanescent modes (Linton 2010):

$$G_\Lambda(\boldsymbol{x},\boldsymbol{y}) = \frac{\mathrm{i}}{2A}\sum_m \frac{1}{\gamma_m} e^{\pm \mathrm{i}\gamma_m x_3}\, e^{\mathrm{i}\boldsymbol{\beta}_m\cdot\boldsymbol{x}'}, \tag{4.11}$$

where $\gamma_m = \sqrt{\kappa^2 - \boldsymbol{\beta}_m^2}$ and $\boldsymbol{\beta}_m = \boldsymbol{\beta} + 2\pi\,(m_1\boldsymbol{\xi}_1^* + m_2\boldsymbol{\xi}_2^*)$, where $(\boldsymbol{\xi}_1^*, \boldsymbol{\xi}_2^*)$ is the dual basis of $(\boldsymbol{\xi}_1, \boldsymbol{\xi}_2)$. With the condition on the lattice (2.6), only the fundamental mode is propagating, so that

$$G_\Lambda(\boldsymbol{x},\boldsymbol{y}) = \frac{\mathrm{i}}{2\kappa A\cos\Phi}\, e^{-\mathrm{i}\kappa\boldsymbol{\tau}'\cdot\boldsymbol{y}'} + \text{ evanescent modes.} \tag{4.12}$$

The reflection and transmission coefficients are hence

$$R_\delta = 1 - \frac{\mathrm{i}Q_\delta^+}{\kappa A\cos\Phi} \text{ and } T_\delta = \frac{\mathrm{i}Q_\delta^-}{\kappa A\cos\Phi}, \tag{4.13}$$

where $Q_\delta^\pm$ are the following fluxes :

$$Q_\delta^\pm = \int_{\mathsf{D}_+} e^{-\mathrm{i}\kappa\boldsymbol{\tau}'\cdot\boldsymbol{y}'}\partial_{x_3} p_\pm(\boldsymbol{y}',0)\,\mathrm{d}\boldsymbol{y}' \tag{4.14}$$

The objective in this section is to adapt the approach in Leppington & Levine (1973) to get a second-order asymptotic expansion for R_δ and T_δ in powers of δ for generic perforations and plates, including thick ones.

Equations (4.7) and (4.8) make it clear that the determination of p, p_+ and p_- only requires solving a problem set solely on the hole Ω. To suppress the dependence of the geometry on δ, it is convenient to introduce the scaled variable

$$\boldsymbol{X} = \boldsymbol{x}/\delta, \tag{4.15}$$

also called a fast (or inner) variable in asymptotic expansions theory. In this way, Ω, Σ and $\widehat{\mathsf{D}}$ are parametrized by fixed sets respectively denoted $\widehat{\Omega}$, $\widehat{\Sigma}$ and $\widehat{\mathsf{D}}_\pm$, meaning that they are independent of δ. Domain $\widehat{\Omega}$ can hence be viewed as an isolated perforation in a plate extending to infinity (see Tuck (1975); Howe (1998)) where this feature is introduced in a quite implicit way and Bendali *et al.* (2012) where it is dealt with by means of a matched asymptotic expansion technique.

The expansion of R_δ and T_δ will be obtained through the second-order asymptotic expansion of the function Π_δ defined on $\widehat{\Omega}$ through the scaling (4.15)

$$p(\delta\boldsymbol{X}) = \Pi_\delta(\boldsymbol{X}) = \Pi^{(0)}(\boldsymbol{X}) + \delta\Pi^{(1)}(\boldsymbol{X}) + o(\delta)\,. \tag{4.16}$$

Clearly, introducing expansion (4.16) into the Helmholtz equation and the boundary condition on Σ yields

$$\begin{cases} \nabla_{\boldsymbol{X}}^2\Pi^{(j)} = 0 & \text{in } \widehat{\Omega} \\ \partial_{\boldsymbol{n}}\Pi^{(j)} = 0 & \text{on } \widehat{\Sigma}, \end{cases} \tag{4.17}$$

for $j = 0, 1$, with $\boldsymbol{n}$ the unit normal to $\widehat{\Sigma}$ directed outwards $\widehat{\Omega}$. The expansion of the integral equations set on respectively D_+ and D_- requires using the theory of lattice sums for the Helmholtz equation, which gives (Linton 2010, page 653)

$$G_\Lambda(\delta\boldsymbol{X},\delta\boldsymbol{Y}) = \frac{1}{4\pi\delta|\boldsymbol{X}'-\boldsymbol{Y}'|} + s_0 + o(\delta)\,, \tag{4.18}$$

where s_0 has an explicit expression in terms of a Schlömilch series, see Linton & Thompson (2009). As a result, expanding

$$p_0(\delta \boldsymbol{X}'_+, 0) = 2e^{\mathrm{i}\kappa\boldsymbol{\tau}'\cdot\boldsymbol{X}'_+} = 2 + 2\delta\mathrm{i}\kappa\boldsymbol{\tau}'\cdot\boldsymbol{X}'_+ + o(\delta), \tag{4.19}$$

and expressing the integral equations of (4.7) in terms of the fast variables, gives

$$\left\{\begin{array}{l} \Pi^{(0)}_+(\boldsymbol{X}'_+) + \displaystyle\int_{\widehat{\mathsf{D}}_+} \frac{\partial_{X_3}\Pi^{(0)}_+(\boldsymbol{Y}')}{2\pi|\boldsymbol{X}'_+ - \boldsymbol{Y}'|}\,\mathrm{d}\boldsymbol{Y}' = 2 \\ \Pi^{(0)}_-(\boldsymbol{X}'_-) - \displaystyle\int_{\widehat{\mathsf{D}}_-} \frac{\partial_{X_3}\Pi^{(0)}_-(\boldsymbol{Y}')}{2\pi|\boldsymbol{X}'_- - \boldsymbol{Y}'|}\,\mathrm{d}\boldsymbol{Y}' = 0 \end{array}\right. \tag{4.20}$$

$$\left\{\begin{array}{l} \Pi^{(1)}_+(\boldsymbol{X}'_+) + \displaystyle\int_{\widehat{\mathsf{D}}_+} \frac{\partial_{X_3}\Pi^{(1)}_+(\boldsymbol{Y}')}{2\pi|\boldsymbol{X}'_+ - \boldsymbol{Y}'|}\,\mathrm{d}\boldsymbol{Y}' = -2s_0\displaystyle\int_{\widehat{\mathsf{D}}_\pm} \partial_{X_3}\Pi^{(0)}\mathrm{d}\boldsymbol{Y}' + 2\mathrm{i}\kappa\boldsymbol{\tau}'\cdot\boldsymbol{X}'_+ \\ \Pi^{(1)}_-(\boldsymbol{X}'_-) - \displaystyle\int_{\widehat{\mathsf{D}}_-} \frac{\partial_{X_3}\Pi^{(1)}_-(\boldsymbol{Y}')}{2\pi|\boldsymbol{X}'_- - \boldsymbol{Y}'|}\,\mathrm{d}\boldsymbol{Y}' = \quad 2s_0\displaystyle\int_{\widehat{\mathsf{D}}_\pm} \partial_{X_3}\Pi^{(0)}\mathrm{d}\boldsymbol{Y}' \end{array}\right. \tag{4.21}$$

where $\Pi^{(j)}_\pm$ stand for the respective expressions of $\Pi^{(j)}$ on $\widehat{\mathsf{D}}_\pm$ in terms of the variables $\boldsymbol{X}'_\pm = \boldsymbol{x}'_\pm/\delta$. Define $\Pi^{(0)}$ in $\widehat{\Omega}$ so that it can be extended by

$$\Pi^{(0)}_+(\boldsymbol{X}'_+) = 2 - \int_{\widehat{\mathsf{D}}_+} \frac{\partial_{X_3}\Pi^{(0)}_+(\boldsymbol{Y}')}{2\pi|\boldsymbol{X}'_+ - \boldsymbol{Y}'|}\,\mathrm{d}\boldsymbol{Y}' \text{ and } \Pi^{(0)}_-(\boldsymbol{X}'_-) = \int_{\widehat{\mathsf{D}}_-} \frac{\partial_{X_3}\Pi^{(0)}_-(\boldsymbol{Y}')}{2\pi|\boldsymbol{X}'_- - \boldsymbol{Y}'|}\,\mathrm{d}\boldsymbol{Y}', \tag{4.22}$$

for $\pm X_3 > 0$, respectively. Actually, equations (4.17) and (4.20) mean that $\Pi^{(0)}$ is the solution of the following boundary-value problem

$$\left\{\begin{array}{ll} \nabla^2_{\boldsymbol{X}}\Pi^{(0)} = 0 & \text{in } \widehat{\Omega} \\ \partial_{\boldsymbol{n}}\Pi^{(0)} = 0 & \text{on } \widehat{\Sigma}, \\ \displaystyle\lim_{X_3\to+\infty} \Pi^{(0)}_+ = 2, & \displaystyle\lim_{X_3\to-\infty} \Pi^{(0)}_- = 0. \end{array}\right. \tag{4.23}$$

This shows that

$$\widehat{K_R} = \frac{1}{2}\int_{\widehat{\mathsf{D}}_\pm} \partial_{X_3}\Pi^{(0)}\mathrm{d}\boldsymbol{Y}'. \tag{4.24}$$

is nothing else than the Rayleigh conductivity of the isolated perforation in the scaled variables (4.15). Coming back to the initial variables, we can express $\widehat{K_R}$ by means of the usual Rayleigh conductivity defined in (3.2)

$$\widehat{K_R} = K_R/\delta. \tag{4.25}$$

In a similar way, $\Pi^{(1)}$ can be expressed from the solution of the following problem

$$\left\{\begin{array}{ll} \nabla^2_{\boldsymbol{X}}\Pi^{\boldsymbol{X}}_l = 0 & \text{in } \widehat{\Omega} \\ \partial_{\boldsymbol{n}}\Pi^{\boldsymbol{X}}_l = 0 & \text{on } \widehat{\Sigma}, \\ \displaystyle\lim_{X_3\to+\infty} \big(\Pi^{\boldsymbol{X}}_l(\boldsymbol{X}) - \boldsymbol{X}'_l\big) = 2, & \displaystyle\lim_{X_3\to-\infty} \Pi^{\boldsymbol{X}}_l(\boldsymbol{X}) = 0, \end{array}\right. \tag{4.26}$$

for $l = 1, 2$ and the previous function $\Pi^{(0)}$ through

$$\Pi^{(1)}(\boldsymbol{X}) = -4s_0\,\widehat{K_R}\,\Pi^{(0)}(\boldsymbol{X}) + 2\mathrm{i}\kappa\boldsymbol{\tau}'\cdot\boldsymbol{\Pi}^{\boldsymbol{X}}(\boldsymbol{X}), \tag{4.27}$$

where $\boldsymbol{\Pi}^{\boldsymbol{X}}$ is the vector function whose components are respectively $\Pi^{\boldsymbol{X}}_1$, $\Pi^{\boldsymbol{X}}_2$ and 0.

The fluxes $Q_\delta^\pm$ defined in equation (4.14) now become, up to some $o(\delta^2)$ terms,

$$\begin{aligned} Q_\delta^\pm &= \delta \int_{\widehat{\mathsf{D}}_\pm} \exp\left(-\mathrm{i}\kappa\delta\boldsymbol{\tau}'\cdot\boldsymbol{Y}'\right)\left(\partial_{X_3}\Pi_\pm^{(0)} + \delta\partial_{X_3}\Pi_\pm^{(1)}\right)(\boldsymbol{Y}'_\pm, 0)\,\mathrm{d}\boldsymbol{Y}' + o(\delta^2) \\ &= 2\delta\widehat{K_R} + \delta^2\int_{\widehat{\mathsf{D}}_\pm}\left(\partial_{X_3}\Pi_\pm^{(1)} - \mathrm{i}\kappa\boldsymbol{\tau}'\cdot\boldsymbol{Y}'\partial_{X_3}\Pi_\pm^{(0)}\right)\mathrm{d}\boldsymbol{Y}' \end{aligned} \tag{4.28}$$

which, thanks to (4.27), gives

$$Q_\delta^\pm = 2\delta\widehat{K_R} + \delta^2\left(2\mathrm{i}\kappa\boldsymbol{\tau}'\cdot\int_{\widehat{\mathsf{D}}_\pm}\left(\partial_{X_3}\boldsymbol{\Pi}_\pm^{\boldsymbol{X}} - \frac{1}{2}\boldsymbol{Y}'\partial_{X_3}\Pi_\pm^{(0)}\right)\mathrm{d}\boldsymbol{Y}' - 8s_0\widehat{K_R}^2\right) \tag{4.29}$$

A reciprocity property (see Bendali *et al.* 2012, page 16) yields

$$\begin{cases} \displaystyle\int_{\widehat{\mathsf{D}}_+}\left(\partial_{X_3}\boldsymbol{\Pi}_+^{\boldsymbol{X}} - \frac{1}{2}\boldsymbol{Y}'_+\partial_{X_3}\Pi_+^{(0)}\right)\mathrm{d}\boldsymbol{Y}'_+ = 0 \\ \displaystyle\int_{\widehat{\mathsf{D}}_-}\left(\partial_{X_3}\boldsymbol{\Pi}_-^{\boldsymbol{X}} - \frac{1}{2}\boldsymbol{Y}'_-\partial_{X_3}\Pi_-^{(0)}\right)\mathrm{d}\boldsymbol{Y}'_- = -\widehat{\mu_n}, \end{cases} \tag{4.30}$$

with

$$\widehat{\mu_n} = (\boldsymbol{c}_+ - \boldsymbol{c}_-)\widehat{K_R} - \frac{1}{2}\int_{\widehat{\Sigma}}\Pi^{(0)}\boldsymbol{n}'\,\mathrm{d}s, \tag{4.31}$$

where $\boldsymbol{c}_\pm = \boldsymbol{X} - \boldsymbol{X}_\pm$ take into account the difference of the centres of phases chosen for the reflected and transmitted waves and $\boldsymbol{n}'$ is the projection of the unit normal $\boldsymbol{n}$ to $\widehat{\Sigma}$ on the plane of the plate. For an axisymmetric perforation, $\widehat{\mu_n}$ reduces to

$$\widehat{\boldsymbol{\mu}_n} = \frac{h}{\delta}\,\widehat{K_R}\boldsymbol{e}_3 = \frac{h\,K_R}{\delta^2}\,\boldsymbol{e}_3, \tag{4.32}$$

where $\boldsymbol{e}_3$ is the unit vector along the x_3-axis.

As a result, the reflection and the transmission coefficients have the following asymptotic expansions, as obtained in (Bendali *et al.* 2012) through a more involved procedure based on the method of matched asymptotic expansions

$$\begin{cases} R_\delta = 1 + \dfrac{\delta\,\widehat{K_R}}{A}\dfrac{2}{\mathrm{i}\kappa\cos\Phi} - \dfrac{\delta^2\,4\,\widehat{K_R}^2\,s_0}{A}\dfrac{2}{\mathrm{i}\kappa\cos\Phi} + o(\delta^2) \\ T_\delta = \quad -\dfrac{\delta\,\widehat{K_R}}{A}\dfrac{2}{\mathrm{i}\kappa\cos\Phi} + \dfrac{\delta^2\left(4\,\widehat{K_R}^2\,s_0 + \mathrm{i}\kappa\boldsymbol{\tau}'\cdot\widehat{\boldsymbol{\mu}_n}\right)}{A}\dfrac{2}{\mathrm{i}\kappa\cos\Phi} + o(\delta^2). \end{cases} \tag{4.33}$$

It is worth mentioning that the term $\boldsymbol{\tau}'\cdot\widehat{\boldsymbol{\mu}_n}$ is equal to zero for an axisymmetric perforation since then $\boldsymbol{\tau}'$ has no component along the x_3-axis.

Finally, in terms of the Rayleigh conductivity in the initial variables, we get

$$\begin{cases} R_\delta = 1 - \dfrac{2\mathrm{i}}{\kappa A\cos\Phi}K_R + \dfrac{8\mathrm{i}s_0}{\kappa A\cos\Phi}K_R^2 + o(\delta^2) \\ T_\delta = \quad \dfrac{2\mathrm{i}}{\kappa A\cos\Phi}K_R - \dfrac{2\mathrm{i}s_0}{\kappa A\cos\Phi}\left(4K_R^2 + \mathrm{i}\kappa\boldsymbol{\tau}'\cdot\boldsymbol{\mu}_n\right) + o(\delta^2). \end{cases} \tag{4.34}$$

4.4. *Effective compliance of the perforated plate*

The effective compliance K of the plate can hence be defined through the following relationships

$$\partial_{x_3}p_+ = \partial_{x_3}p_- = K(p_+ - p_-). \tag{4.35}$$

The reflection and transmission coefficients and the compliance are then linked by

$$R+T=1, \quad K=\frac{\mathrm{i}\kappa\cos\Phi}{2}\left(1-\frac{1}{R}\right), \quad R=1/\left(1-\frac{2K}{\mathrm{i}\kappa\cos\Phi}\right) \tag{4.36}$$

Moreover, if, as here, the governing equations are those of linear acoustics, which means that no damping mechanism is involved and that there is no acoustic absorption by the perforated plate, the imaginary part $\mathrm{Im}(K)$ of the effective compliance is zero and the conservation of energy is expressed through the following relation

$$1-|R|^2-|T|^2=0. \tag{4.37}$$

Clearly, if R_δ and T_δ are approximated at first order from equation (4.33) or (4.34)

$$\begin{cases} R_\delta^{(1)} = 1+\dfrac{\delta\,\widehat{K_R}}{A}\dfrac{2}{\mathrm{i}\kappa\cos\Phi} = 1-\dfrac{2\mathrm{i}}{\kappa A\cos\Phi}K_R \\ T_\delta^{(1)} = \quad -\dfrac{\delta\,\widehat{K_R}}{A}\dfrac{2}{\mathrm{i}\kappa\cos\Phi} = \quad -\dfrac{2\mathrm{i}}{\kappa A\cos\Phi}K_R \end{cases} \tag{4.38}$$

then equation (4.37) is not satisfied. Even worse, the reflected wave is amplified

$$|R_\delta^{(1)}| = \sqrt{1+\left(\frac{K_R}{A}\frac{2}{\kappa\cos\Phi}\right)^2} \tag{4.39}$$

and the imaginary part of the effective compliance associated with these coefficients

$$K_\delta^{(1)} = \frac{\delta\,\widehat{K_R}/A}{1+\dfrac{\delta\,\widehat{K_R}}{A}\dfrac{2}{\mathrm{i}\kappa\cos\Phi}} \tag{4.40}$$

is not zero. However, it is possible to write this compliance slightly differently, so that the compliance is both consistent with the approximation of the effective reflection and transmission coefficients at leading order $O(\delta)$, and ensures the conservation of acoustic energy:

$$K_\delta^{(1)} = \frac{\delta\,\widehat{K_R}}{A} = \frac{K_R}{A} \tag{4.41}$$

We thus obtain the classical expression of the effective compliance of the perforated plate (Eldredge & Dowling 2003; Hughes & Dowling 1990). The reflection coefficient corresponding to this compliance condition

$$R_\delta^{(1)} = \frac{1}{1-\dfrac{2}{\mathrm{i}\kappa\cos\Phi}\dfrac{K_R}{A}}. \tag{4.42}$$

does not lead to an amplified reflected wave while approximating the actual reflection coefficient up to a term in $o(\delta)$.

In general, the same procedure cannot be repeated to get a second-order compliance condition since the term $\boldsymbol{\tau}'\cdot\widehat{\boldsymbol{\mu}_n}$ in equations (4.33) or (4.34) prevents the condition $R+T=1$ from being satisfied. However, this can be done when $\boldsymbol{\tau}'\cdot\widehat{\boldsymbol{\mu}_n}=0$, for instance when the perforation is axisymmetric or when the thickness of the plate can be neglected.

Then, equations (4.33) or (4.34) read at second order in δ:

$$\left\{\begin{array}{lll} R_\delta^{(2)} & = 1 + \dfrac{2}{\mathrm{i}A\kappa\cos\Phi}\left(\delta\,\widehat{K_R} - \delta^2 4s_0\,\widehat{K_R}^2\right) = 1 - \dfrac{2\mathrm{i}\,K_R\,(1-4s_0\,K_R)}{A\kappa\cos\Phi} \\ T_\delta^{(2)} & = -\dfrac{2}{\mathrm{i}A\kappa\cos\Phi}\left(\delta\,\widehat{K_R} - \delta^2 4s_0\widehat{K_R}^2\right) = \dfrac{2\mathrm{i}\,K_R\,(1-4s_0\,K_R)}{A\kappa\cos\Phi}. \end{array}\right. \tag{4.43}$$

Therefore, the associated compliance is:

$$K_\delta^{(2)} = \frac{\dfrac{\delta\widehat{K_R}}{A}\left(1-4s_0\delta\,\widehat{K_R}\right)}{1+\dfrac{2}{\mathrm{i}\kappa\cos\Phi}\dfrac{\delta\widehat{K_R}}{A}\left(1-4s_0\delta\,\widehat{K_R}\right)} = \frac{K_R\,(1-4s_0\,K_R)\,/A}{1+\dfrac{2\,K_R\,(1-4s_0\,K_R)}{\mathrm{i}A\kappa\cos\Phi}}. \tag{4.44}$$

As for (4.40), this compliance does not conserve energy. However, consistently with the order in $O(\delta^2)$ of the approximation of R_δ and T_δ, equation (4.44) is equivalent to:

$$\begin{aligned} K_\delta^{(2)} &= \frac{\delta\widehat{K_R}}{A}\left(1-4s_0\delta\,\widehat{K_R}\right)\left(1-\frac{2}{\mathrm{i}\kappa\cos\Phi}\frac{\delta\widehat{K_R}}{A}\left(1-4s_0\delta\,\widehat{K_R}\right)\right) \\ &= \frac{\delta\widehat{K_R}}{A}\left(1-2\delta\,\widehat{K_R}\left(2s_0-\frac{\mathrm{i}}{\kappa\cos\Phi}\right)\right). \end{aligned} \tag{4.45}$$

A very far-reaching, by no means obvious, property of the lattice sums for the Helmholtz equation (see Linton 2010, page 656) ensures that

$$\mathrm{Im}\,(2s_0) = \frac{1}{\kappa\cos\Phi}. \tag{4.46}$$

As a result, the compliance at order 2 is given by

$$K_\delta^{(2)} = \frac{K_R}{A}\left(1-4K_R\mathrm{Re}(s_0)\right). \tag{4.47}$$

The coefficient $\mathrm{Re}(s_0)$ adds a correction depending on the shape of the array of the perforations rather than just averaging by the area A of the lattice unit cell. The corresponding reflection coefficient

$$R_\delta^{(2)} = \left(1+\frac{2\mathrm{i}}{\kappa\cos\Phi}\frac{K_R}{A}\left(1-4K_R\mathrm{Re}(s_0)\right)\right)^{-1} \tag{4.48}$$

does not exhibit any unrealistic behaviour. Leppington and Levine gave a similar expression for a rectangular lattice of elliptical holes (see Leppington & Levine 1973, equation (2.27)). The approximation (4.48) of the reflection coefficient is an extension of this formula to an arbitrary shape of the lattice and to any geometry of the perforations, if either the plate is infinitely thin or the perforations are axisymmetric. Otherwise, second-order terms in $O(\delta^2)$ are missed.

4.5. *Numerical results for a generic plate*

Some numerical experiments can now be conducted to illustrate the influence of the geometry of the perforations and the shape of the lattice for a realistic configuration of the perforated plate. A 2mm-thick perforated plate of 1.96% porosity is considered, with either a rectangular or staggered lattice of holes. As in section 3.4.1, the characteristic size of the holes is $r = 0.225$mm. The incidence of the incoming acoustic wave is $\Phi = 45^o$. The dimensions of the lattice are $|\boldsymbol{\xi}_1| = 3$mm and $|\boldsymbol{\xi}_2| = 2.7$mm in the rectangular configuration, $|\boldsymbol{\xi}_1| = 3$mm and $|\boldsymbol{\xi}_2| = \sqrt{(1.5)^2+(2.7)^2} \approx 3.1$mm in the staggered one.

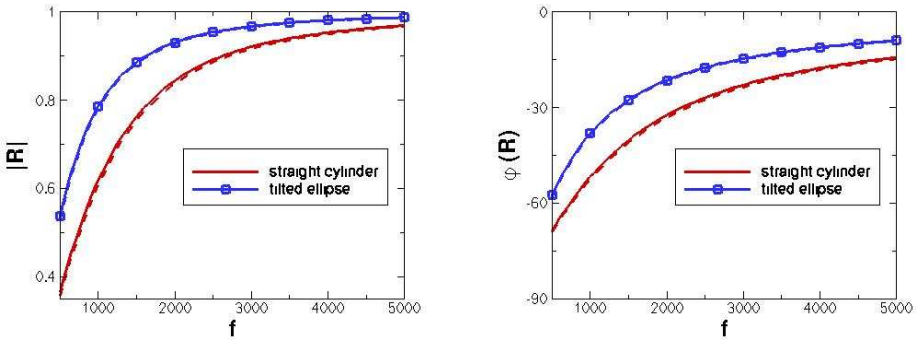

(a) Amplitude (b) Phase (in degrees)

Figure 10: Reflection coefficient of the perforated plate with a rectangular lattice of untilted cylindrical perforations (red lines without symbols) or tilted perforations with an elliptical section (blue lines with symbols). First order approximations are plotted in solid lines, second order ones in dashed lines.

Thus, the surface of the lattice cell is the same in both configurations, i.e., $A = 8.1\text{mm}^2$. The assumption that $\delta = r/L$ is a small parameter is satisfied.

Here, we focus on two kinds of geometries for the holes: the untilted cylinder of radius r and the tilted ellipse with circular bore of radius r and a 60^o tilt angle. The mean value of the bounds (3.8) and (3.31) are taken as the respective Rayleigh conductivities of these perforations. As discussed in section 4.4, the reflection coefficient can be computed at first and second order in δ by equations (4.42) and (4.48), respectively.

Results in the frequency range $[500, 5000]$Hz are plotted in figure 10, for the rectangular lattice. The geometry of the perforations has a strong effect on the reflection coefficient, which confirms the importance of using the expressions for the Rayleigh conductivity obtained in section 3. On the contrary, first and second order approximations are almost indistinguishable, which shows that the usual way of calculating the effective compliance of the plate (i.e., by averaging the Rayleigh conductivity of the isolated hole by the area of the lattice unit cell) is quite accurate in this case.

Consequently, it seems obvious that changing the shape of the lattice will not affect the reflection coefficient significantly. This is shown in figure 11, which depicts the deviation of the staggered array from the rectangular one expressed as a percentage of the latter.

For both geometries of the perforations and whatever the frequency, the reflection coefficients differ from each other by less than 0.02%. This means that the shape of the lattice can be neglected without reducing the quality of the models, and that considering first-order usual approximations for the reflection and the transmission coefficients is sufficient.

5. Conclusion

The acoustic properties of a low-porosity perforated plate in a compressible ideal inviscid fluid have been investigated in the absence of mean flow. This generalizes previous work of Leppington & Levine (1973) to account for thick plates with perforations of arbitrary arrangement and various geometries. The study was conducted in two stages. As a first step, we developed a mathematical framework yielding accurate bounds of the Rayleigh conductivity for realistic geometric configurations, including tilted perfora-

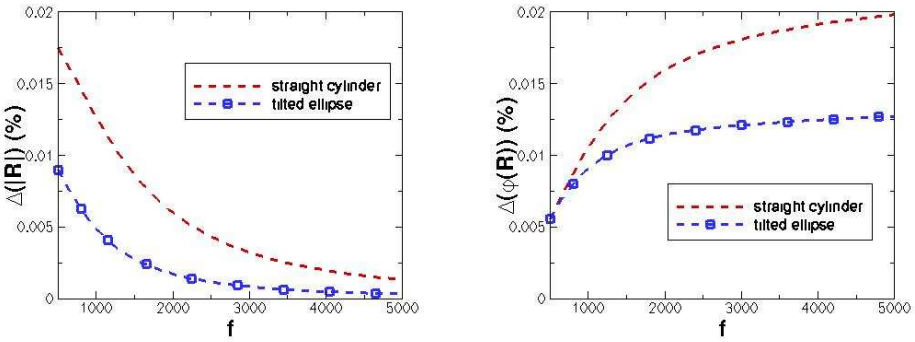

(a) Amplitude (b) Phase

Figure 11: Difference between the second-order reflection coefficient in the staggered and rectangular arrangement of the holes, normalized by the rectangular arrangement value.

tions. We then used a domain decomposition concept, coupled with an integral equation method, the theory of lattice sums for the Helmholtz equation and the asymptotic expansions method to significantly extend previous approaches which were either intuitive or rigorous in order to derive effective parameters for the acoustic properties of a multi-perforated plate.

In section 3, we focused on the Rayleigh conductivity of a single perforation, which can be related to the inertial end correction used in impedance models. Lord Rayleigh (1945) gave two bounds for the conductivity of a circular aperture of zero-thickness, and his work was extended to thick cylindrical perforations by Howe (1998). These expressions are nowadays widely used in impedance and conductivity models, even when perforations of other geometries are considered. We have shown here that these lower and upper bounds can be obtained by applying of the Dirichlet and Kelvin variational principles. This rigorous mathematical framework allows computation of the lower and upper bounds of the Rayleigh conductivity for various geometries of the perforation. We investigated untilted perforations with either a conical shape or an elliptical section, as well as tilted perforations of circular and elliptical sections. The latter case is of primary interest for industrial applications, especially in the domain of engine combustors where walls are perforated by sub-millimeter tilted apertures for cooling purposes. In related theoretical or numerical studies, some researchers use the Rayleigh conductivity (or end correction) of a untilted cylindrical aperture with a modified plate thickness which corresponds to the length of the centerline of the tilted aperture. Our analysis has given exact bounds for the Rayleigh conductivity and end correction in such geometrical configurations and has shown that these quantities were quite sensitive to the tilt angle and that the thickness effect requires a more precise calculation than just considering the intuitive effective thickness. It should be noted that though we have only considered the Rayleigh conductivity in the framework of the purely acoustic problem, i.e. without any flow or non-linear effects, this solution can be used as the groundwork for deriving Rayleigh conductivity in the presence of a bias flow through the aperture, as was done by Howe (1979) from the Rayleigh conductivity of a thin circular aperture. We have thus shown that in the study of a bias flow through a tilted perforation carried out by Eldredge *et al.* (2007), a better match between the theoretical model and the numerical simulations could have been obtained if the exact expression of the Rayleigh conductivity had been used.

Then, in section 4, we performed an asymptotic expansion on the scattering problem

with respect to the small ratio δ between the characteristic sizes of the perforation and of the lattice cell. We derived accurate first-order and second-order expansions of the reflection and transmission coefficients, which are expressed in terms of the Rayleigh conductivity of the perforation. These expressions extend those previously given by Leppington & Levine (1973): they are valid for thick plates with an arbitrary grating of perforations with various geometries. It should be noted that the only constraint required on the size of the lattice cell is that it has to be smaller than half of the acoustic wavelength, contrary to the conventional long wavelength assumption. Moreover, we have shown that it is necessary to modify the $O(\delta)$ and $O(\delta^2)$ expansions of the reflection and transmission coefficients to ensure the conservation of acoustic energy. Thus, the asymptotics provide a first-order and second-order expression of the effective compliance of the perforated plate. The first-order-accurate compliance is the same as the classical expression, i.e. the averaging of the Rayleigh conductivity of a single peforation by the area of the lattice unit cell. The accurate second-order compliance involves corrections by a coefficient that depends on the shape of the lattice. Finally, numerical calculations on a generic plate have shown that the second-order corrections, and therefore the effects of the lattice shape, can be neglected without loss of accuracy.

Acknowledgements

Part of this work was supported by the French National Research Agency (ANR) under grant no. ANR−08−SYSC−001.

Appendix A. Functions involved in the Dirichlet and Kelvin principles

This appendix is dedicated to the calculations described in sections 3.2 and 3.3. To obtain bounds for the Rayleigh conductivity, suitable test functions ψ and $\boldsymbol{q}$ are required to minimize (respectively maximize) the functional J_1 (respectively J_2) of (3.7). To do so, auxiliary problems, depending on the geometry of the aperture, have to be solved.

Untilted apertures

For a cylindrical perforation of radius R, the problem is as follows:

$$\begin{cases} \Delta w_R(\boldsymbol{x}) = 0, & \text{for } x_3 \neq \pm h/2, \\ \partial_{x_3} w_R(x_1, x_2, 0) = 0, & \text{for } x_1^2 + x_2^2 > R^2, \\ w_R(x_1, x_2, 0) = 1/2, & \text{for } x_1^2 + x_2^2 < R^2. \end{cases} \tag{A 1}$$

Its solution satisfies

$$\int_{\pm x_3 > h/2} \left| \boldsymbol{\nabla} w_R(\boldsymbol{x}) \right|^2 \mathrm{d}\boldsymbol{x} = R. \tag{A 2}$$

This integral is directly involved in the computation of the functional J_1 (used to obtain the sought upper bound). The explicit expression of w_R is not required. The proof of (A 2) is given in Laurens *et al.* (2012), as well as the explicit expression of w_R under an integral form. For $\alpha \in \mathbb{R}$, the correct test function ψ is defined as

$$\psi(\boldsymbol{x}) = \begin{cases} \pm 1/2 \mp (1 \mp 2\alpha)\, w_R(x_1, x_2, x_3 \mp h/2), & \text{for } \pm x_3 > h/2, \\ \alpha, & \text{for } -h/2 < x_3 < h/2. \end{cases} \tag{A 3}$$

The lower bound is based on the following problem:

$$\begin{cases} \Delta z_R(\boldsymbol{x}) = 0, & \text{for } x_3 \neq \pm h/2, \\ \partial_{x_3} z_R(x_1, x_2, 0) = 0, & \text{for } x_1^2 + x_2^2 > R^2, \\ \partial_{x_3} z_R(x_1, x_2, 0_\pm) = \pm 1, & \text{for } x_1^2 + x_2^2 < R^2. \end{cases} \tag{A 4}$$

Its solution satisfies

$$\int_{\pm x_3 > h/2} \left| \boldsymbol{\nabla} z_R(\boldsymbol{x}) \right|^2 \, \mathrm{d}\boldsymbol{x} = 8R^3/3. \tag{A 5}$$

For $\beta \in \mathbb{R}$, the suitable test function for J_2 is

$$\boldsymbol{q}(\boldsymbol{x}) = \begin{cases} \pm\beta \, \boldsymbol{\nabla} z_R(x_1, x_2, x_3 \mp h/2) \,/\, \pi R^2, & \text{for } \pm x_3 > h/2, \\ \beta \, \boldsymbol{e}_3 \,/\, \pi R^2, & \text{for } -h/2 < x_3 < h/2. \end{cases} \tag{A 6}$$

In the case of a conical aperture with a radius linearly varying from R_- to R_+, the test function ψ, which is adequate for this geometry, is given by

$$\psi(\boldsymbol{x}) = \begin{cases} \pm 1/2 \mp (1 \mp 2\alpha_\pm) \, w_{R_\pm}(x_1, x_2, x_3 \mp h/2), & \text{for } \pm x_3 > h/2, \\ \alpha_- + \left(\alpha_+ - \alpha_-\right) \dfrac{\int_{-h/2}^{x_3} \frac{dx_3}{\pi R^2(x_3)}}{\int_{-h/2}^{h/2} \frac{dx_3}{\pi R^2(x_3)}}, & \text{for } -h/2 < x_3 < h/2, \end{cases} \tag{A 7}$$

where $w_{R_\pm}$ is the function w_R defined in equation (A 1) with $R = R_\pm$ and $\alpha_\pm$ two real constants.

The lower bound involves the following vector field $\boldsymbol{q}$, with $\beta \in \mathbb{R}$

$$\boldsymbol{q}(\boldsymbol{x}) = \begin{cases} \pm \dfrac{\beta}{\pi \, R_+^2} \, \boldsymbol{\nabla} z_{R_\pm}(x_1, x_2, x_3 \mp h/2) & \text{for } \pm x_3 > h/2, \\ \dfrac{\beta}{\pi \, R^2(x_3)} \left(\boldsymbol{e}_3 + \dfrac{r}{R(x_3)} \dfrac{R_+ - R_-}{h} \boldsymbol{e}_r \right) & \text{for } -h/2 < x_3 < h/2, \end{cases} \tag{A 8}$$

and $z_{R_\pm}$ defined as in equation (A 4) with $R = R_\pm$.

For an elliptical section, problems (A 1) and (A 4) are posed on the ellipse A, instead on the disc of radius R. The solution of these problems will be denoted by $\widetilde{w_R}$ and $\widetilde{z_R}$ respectively. They are such that

$$\int_{\pm x_3 > h/2} \left| \boldsymbol{\nabla} \widetilde{w_R}(\boldsymbol{x}) \right|^2 \mathrm{d}\boldsymbol{x} = \pi a \frac{K(0)}{K(\varepsilon)} \text{ and } \int_{\pm x_3 > h/2} \left| \boldsymbol{\nabla} \widetilde{z_R}(\boldsymbol{x}) \right|^2 \, \mathrm{d}\boldsymbol{x} = \frac{8}{3} ab^2 \frac{K(\varepsilon)}{K(0)}. \tag{A 9}$$

More details can be found in Laurens & Tordeux (February 2013).

Tilted apertures

If the aperture is cylindrical and tilted with an angle θ, a new auxiliary problem has to be considered

$$\begin{cases} \Delta t_R(\boldsymbol{x}) = 0, & \text{for } x_3 \neq \pm h/2, \\ \partial_{x_3} t_R(x_1, x_2, 0) = 0, & \text{for } x_1^2 + x_2^2 > R^2, \\ t_R(x_1, x_2, 0) = x_1, & \text{for } x_1^2 + x_2^2 < R^2, \end{cases} \tag{A 10}$$

with

$$\int_{\pm x_3 > h/2} \left| \boldsymbol{\nabla} t_R(\boldsymbol{x}) \right|^2 \, \mathrm{d}\boldsymbol{x} = 8R^3/3. \tag{A 11}$$

The test function ψ is therefore

$$\psi(\boldsymbol{x}) = \begin{cases} \pm 1/2 \mp (1 \mp 2\alpha)\ w_R(\widehat{x}_1, x_2, x_3 \mp h/2) \\ \qquad + \dfrac{\mu_\alpha\ \sin\theta}{h}\ t_R(\widehat{x}_1, x_2, x_3 \mp h/2), & \text{for } \pm x_3 > h/2, \\ -\alpha + \dfrac{\mu_\alpha}{h}\Big((x_3 + h/2)\ \cos\theta + x_1\ \sin\theta\Big), & \text{for } -h/2 < x_3 < h/2, \end{cases} \tag{A 12}$$

with α real constant and $\mu_\alpha = 2\alpha\ \cos\theta$ and $\widehat{x}_1(\boldsymbol{x}) = x_1 - (x_3 + h/2)\ \tan\theta$.
The lower bound is established by chosing

$$\boldsymbol{q}(\boldsymbol{x}) = \begin{cases} \pm\dfrac{\beta}{\pi\ R^2}\ \boldsymbol{\nabla} z_R(\widehat{x}_1, x_2, x_3 \mp h/2) & \text{for } \pm x_3 > h/2, \\ \dfrac{\beta}{\pi\ R^2}\ \Big(\boldsymbol{e}_3 + \tan\theta\ \boldsymbol{e}_1\Big) & \text{for } -h/2 < x_3 < h/2, \end{cases} \tag{A 13}$$

with β a real constant.

For the elliptic case, problem (A 10) is set on an ellipse A instead of the disc. Thus, the solution of this problem, denoted $\widetilde{t_R}$, is different and such that

$$\int_{\pm x_3 > h/2} \left|\boldsymbol{\nabla}\widetilde{t_R}(\boldsymbol{x})\right|^2\ \mathrm{d}\boldsymbol{x} = \frac{8}{3} a^3 \frac{D(0)}{D(\varepsilon)}, \tag{A 14}$$

with $D(\varepsilon)$ defined in (3.27). The test functions ψ and $\boldsymbol{q}$ are similar to (A 12) and (A 13).

REFERENCES

Abrahams, I. D. 1999 Sound radiation from a line forced perforated elastic sandwich panel. *J. Acoust. Soc. Am.* **105** (6), 3009–3020.

Allard, J. F. 1993 *Propagation of Sound in Porous Media*. Elsevier Applied Sciences.

Andreini, A., Bianchini, C., Facchini, B. & Simonetti, F. 2011 Assessment of numerical tools for the evaluation of the acoustic impedance of multi-perforated plates. In *Proceedings of ASME Turbo Expo 2011*. Vancouver, British Columbia, Canada.

Atalla, N. & Sgard, F. 2007 Modeling of perforated plates and screens using rigid frame porous models. *J. Sound Vib.* **303**, 195–208.

Bellucci, V., Flohr, P. & Paschereit, C. O. 2004 Numerical and experimental study of acoustic damping generated by perforated screens. *AIAA Journal* **42** (8), 1543–1549.

Bendali, A., Fares, M.B., Piot, E. & Tordeux, S. 2012 Mathematical justification of the Rayleigh conductivity model for perforated plates in acoustics. *to appear in SIAM Journal on Applied Mathematics* .

Beranek, L. L. 1992 *Noise and Vibration Control Engineering*. Wiley, New York.

Courant, R. & Hilbert, D. 1953 *Methods of mathematical physics. Vol. I*. Interscience Publishers, Inc., New York, N.Y.

Cummings, A. 1984 Acoustic nonlinearities and power losses at orifices. *AIAA Journal* **22**, 786–792.

Cummings, A. 1986 The effects of grazing turbulent pipe-flow on the impedance of an orifice. *Acustica* **61**, 233–242.

Cummings, A. 1987 The response of a resonator under a turbulent boundary layer to a high amplitude non-harmonic sound field. *J. Sound Vib.* **115** (2), 321–328.

Dowling, A. P. & Hughes, I. J. 1992 Sound absorption by a screen with a regular array of slits. *J. Sound Vib.* **156** (3), 387–405.

Eldredge, J. D., Bodony, D. J. & Schoeybi, M. 2007 Numerical investigation of the acoustic behavior of a multi-perforated liner. In *13the AIAA/CEAS Aeroacoustics Conference, AIAA paper 2007-3683*.

Eldredge, J.D. & Dowling, A.P. 2003 The absorption of axial acoustic waves by a perforated liner with bias flow. *J. Fluid Mech.* **485**, 307–335.

Fok, V. A. 1941 Alternatively, see s. n. rschevkin 1963 a course of lectures on the theory of sound. london: Pergamon press. *Doklady Akademii nauk SSSR* **31**.

Guess, A. W. 1975 Calculation of perforated plate liner parameters from specified acoustic resistance and reactance. *J. Sound Vib.* **40** (1), 119–137.

Howe, M. S. 1979 On the theory of unsteady high Reynolds number flow through a circular aperture. *Proc. R. Soc. Lond.* **366**, 205–223.

Howe, M. S. 1980 The influence of vortex shedding on the diffraction of sound by a perforated screen. *J. Fluid Mech.* **97**, 641–653.

Howe, M. S. 1996 The influence of tangential mean flow on the Rayleigh conductivity of an aperture. *Proc. R. Soc. Lond.* **452**, 2303–2317.

Howe, M. S. 1998 *Acoustics of fluid-structure interaction*.

Hughes, I. J. & Dowling, A. P. 1990 The absorption of sound by perforated linings. *J. Fluid Mech.* **218**, 299–335.

Ingard, K. U. 1994 *Notes on Sound Absorption Technology*. Noise Control Foundation, New York.

Ingard, U. 1953 On the theory and design of acoustic resonators. *J. Acoust. Soc. Am.* **25**, 1037–1061.

Jing, X. & Sun, X. 1999 Experimental investigations of perforated liners with bias flow. *J. Acoust. Soc. Am.* **106** (5), 2436–2441.

Jing, X. & Sun, X. 2000 Effect of plate thickness on impedance of perforated plates with bias flow. *AIAA Journal* **38** (9), 1573–1578.

Kirby, R. & Cummings, A. 1998 The impedance of perforated plates subjected to grazing gas flow and backed by porous media. *J. Sound Vib.* **217** (4), 619–636.

Laurens, S. & Tordeux, S. February 2013 Explicit computation of the electrostatic energy for an elliptical charged disc. *Applied Mathematical Letters* **26**, 301305.

Laurens, S., Tordeux, S., Bendali, A., Fares, M. & Kotiuga, R. 2012 Lower and upper bounds for the Rayleigh conductivity of a perforated plate. *under revision for Mathematical Modelling and Numerical Analysis, http://hal.archives-ouvertes.fr/hal-00686438/* .

Lee, S. H., Ih, J. G. & Peat, K. S. 2007 A model of the acoustic impedance of perforated plates with bias flow considering the interaction effect. *J. Sound Vib.* **303**, 741–752.

Lefebvre, A. H. 1999 *Gas Turbines Combustion*. Taylor and Francis.

Leppington, F. G. 1990 The effective boundary conditions for a perforated elastic sandwich panel in a compressible fluid. *Proc. R. Soc. London, Ser. A* **427**, 385–399.

Leppington, F. G. & Levine, H. 1973 Reflexion and transmission at a plane screen with periodically arranged circular or elliptical apertures. *J. Fluid Mech.* **61**, 109–127.

Linton, C.M. 2010 Lattice sums for the Helmholtz equation. *SIAM review* **52** (4), 630–674.

Linton, C.M. & Thompson, I. 2009 One-and two-dimensional lattice sums for the three-dimensional helmholtz equation. *Journal of Computational Physics* **228** (6), 1815–1829.

Luenberger, D.G. 1997 *Optimization by vector space methods*. Wiley-Interscience.

Luong, T., Howe, M. S. & McGowan, R. S. 2005 On the Rayleigh conductivity of a bias-flow aperture. *Journal of Fluids and Structures* **21**, 769–778.

Maa, D. Y. 1998 Potential of microperforated panel absorber. *J. Acoust. Soc. Am.* **104** (5), 2861–2866.

Melling, T. H. 1973 The acoustic impedance of perforates at medium and high sound pressure levels. *J. Sound Vib.* **29** (1), 1–65.

Mendez, S. & Eldredge, J. D. 2009 Acoustic modeling of perforated plates with bias flow for large-eddy simulations. *Journal of Computational Physics* **228**, 4757–4772.

Morfey, C. L. 1969 Acoustic properties of openings at low frequencies. *J. Sound Vib.* **9**, 357–366.

Nedelec, JC & Starling, F. 1991 Integral equation methods in a quasi-periodic diffraction problem for the time-harmonic Maxwell's equations. *SIAM Journal on Mathematical Analysis* **6**, 1679–1701.

Rayleigh, Lord 1945 *The Theory of Sound*, , vol. 2. Dover publications, New York.

Roberts, J.E. & Thomas, J.-M. 1991 Mixed and hybrid methods. In *Handbook of numerical analysis. Vol. 2*. Elsevier Science Publishers.

Scarpato, A., Tran, N., Ducruix, S. & Schuller, T. 2012 Modeling the damping properties

of perforated screens traversed by a bias flow and backed by a cavity at low Strouhal number. *J. Sound Vib.* **331** (2), 276–290.

Sun, X., Jing, X., Zhang, H. & Shi, Y. 2002 Effect of grazing-bias flow interaction on acoustic impedance of perforated plates. *J. Sound Vib.* **254** (3), 557–573.

Tam, C. K. W., Ju, H. & Walker, B. E. 2008 Numerical simulation of a slit resonator in a grazing flow under acoustic excitation. *J. Sound Vib.* **313**, 449–471.

Tuck, E.O. 1975 Matching problems involving flow through small holes. *Advances in applied mechanics* **15**, 89–158.

Yu, J., Kwan, H. W, Echternach, D. K, Kraft, R. E & Syed, A. A 1999 Acoustic treatment design scaling method. *Tech. Rep.*. NASA/CR-1999-209120/VOL3.